

Binder Jet Printing of Stainless Steel 316L

By TUD & CONCR3DE

Diploma Thesis

Jianzhang Wu

Delft University of Technology



Binder Jet Printing of Stainless Steel 316L

by

Jianzhang Wu

<u>Student Name</u>	<u>Student Number</u>
Jianzhang Wu	5470188

Supervisors: Dr. Vera Popovich
Dr. Farid Salari
Thesis Committee: Dr. Vera Popovich
Dr. Farid Salari
Dr. Marcel Hermans
Defence Date: 2025/02/21
Department: Materials Science and Engineering, ME, TU Delft

Acknowledgement

First and foremost, I would like to express my deepest gratitude to Concr3de for providing me with this incredible opportunity. Working hands-on with an industrial 3D printer has allowed me to gain a profound understanding of the entire printing process and its underlying principles from the ground up, while also honing my skills in operating the machine. This invaluable experience has significantly deepened my passion for 3D printing, particularly in industrial applications beyond consumer-grade printers.

I would also like to extend my sincere thanks to my two supervisors, Dr. Vera Popovich from TU Delft and Dr. Farid Salari from Concr3de. I am especially grateful to Vera for her understanding and support, not only in addressing the challenges I faced in my work but also in providing much-needed psychological encouragement. Her guidance has helped me approach difficulties with calmness and confidence. Similarly, a special thanks to Saskia for her thoughtful advice in various aspects of my work, which I found incredibly beneficial.

I am equally thankful to my colleagues at Concr3de who supported me during this project. Whether it was Sergi and Arine, who have since moved on, or Kostyan, Peter, Glenn, Andrey, Rutger, Javier, Henri, Danny, and those in management—Matbaldassari, Eric, Oscar, Mark, and others—your assistance and care made the long hours of waiting for printing processes far more enjoyable and less monotonous.

A special acknowledgment goes to my three close collaborators, former colleagues, and companions: Mannan, Bradley, and Jasper. I greatly appreciated the time we spent working and having fun together—it was truly a highlight of my experience.

Last but not least, Hans, I would like to express my special gratitude to him. Despite his busy schedule, he always managed to organize my experiments meticulously. And our discussions are always highly insightful and inspiring to me.

Finally, I would like to once again express my heartfelt gratitude to Vera. Your unwavering support and guidance have been instrumental in the completion of this thesis.

Abstract

Binder jet printing (BJP) offers a cost-effective and highly efficient alternative to other additive manufacturing techniques. The engineering performance of printed parts is positively correlated with their densification. However, achieving high-density components for 316L stainless steel via BJP remains challenging, as numerous factors during both the printing and post-processing stages can influence the final density of the samples.

In this study, a printer and a proprietary binder developed by Concr3de were employed to fabricate samples using two sizes of 316L stainless steel powders ($<18\ \mu\text{m}$ and $<25\ \mu\text{m}$). Following the standard workflow of printing, debinding, and sintering, various samples were produced by adjusting the printing and sintering parameters. Through characterization and comparative analysis, several key findings and conclusions were drawn.

The sintering process and density were examined, revealing that when the sintering curve included debinding at 450°C for 5 hours followed by sintering at 1400°C or 1410°C for another 5 hours, the sample density stabilized at approximately 94%, with peak values reaching around 98%. This provides a theoretical basis for future post-processing of BJP-manufactured 316L stainless steel samples in industrial applications.

Mechanical properties and shrinkage were also analyzed, showing that the mechanical properties (e.g., hardness) of the samples varied significantly under different sintering atmospheres. Additionally, the shrinkage rate perpendicular to the printing direction (N-direction) reached up to approximately 21% after sintering. Analysis of the printing process, combined with comparisons to other studies, suggests that the green parts in the N-direction exhibit a significant amount of compressible space, indicating that the current printing process leaves room for improvement in the densification of green parts.

Microstructural observations using SEM and OM revealed the presence of voids within the samples. These voids are suspected to be Type III pores during the sintering process.

Key Words: Binder jet printing, 316L stainless steel, sintering, densification

Contents

Acknowledgement	i
Abstract	ii
Nomenclature	viii
1 Introduction	1
1.1 Study Objectives	2
1.2 Project Limitations	3
1.3 Thesis Structure	3
2 Literature Background	5
2.1 Development of Binder Jet Printing	5
2.2 Printing Process	6
2.2.1 Powder Preparation	7
2.2.2 Curing and depowdering	9
2.3 Post Processing	9
2.3.1 Debinding	9
2.3.2 Sintering	10
2.4 Important Parameters	11
2.4.1 Powder Related Parameters	11
2.4.2 Printing Process Parameters	13
2.4.3 Post-Processing Parameters	16
2.5 316L Stainless Steel and BJP	17
3 Methodology	20
3.1 Powder and Binder	20
3.2 Printing and Curing	21
3.3 Debinding and Sintering	23
3.4 Characterization	24
3.4.1 Dimension Test Equipment	24
3.4.2 Density Test Equipment	26
3.4.3 XRD	26
3.4.4 SEM and OM	27
3.4.5 Mechanical Properties Test	27
4 Results and Discussion	28
4.1 Optimization of Green Body Printing Parameters	28
4.1.1 Printing of Green Body	28
4.1.2 Effect of Printing Equipment	31
4.1.3 Calibration of Printing Parameters	33
4.2 Densification of Green Body	35
4.2.1 Effect of Sintering Temperature	35
4.2.2 Effect of Debinding and Sintering Atmosphere	36
4.3 Microstructural Characterization	37
4.3.1 XRD	37
4.3.2 Microstructure	38
4.4 Densification Analysis	43
4.4.1 Density	43
4.4.2 Dimensional Changes	44
4.5 Mechanical Analysis	45
4.5.1 Hardness	45

4.5.2	Compression Tests	48
5	Conslusions	51
6	Knowledge Gap and Further Research	53
6.1	Knowledge gap	53
6.2	Future Research	53
	References	55
A	Printing Parameters	61
B	Image of Samples	62
C	EDS Mapping	64

List of Figures

2.1	Process flow of binder jetting printing[23]	5
2.2	Development of BJP technique[24]	6
2.3	Schematic diagram of binder jetting system[26]	7
2.4	Steps of sample production by BJP[27]	7
2.5	Indirect processing of metal and ceramic powders using PBF[30]	8
2.6	Sintering model[38]	10
2.7	Micrographs of gas-atomized Inconel 718 powders (a) $7\mu\text{m}$, (b) $21\mu\text{m}$,(3) $70\mu\text{m}$ [54]	12
2.8	Measurement of powder bed density: (a) Cups/Fences printing, (b) Tubes insertion,(3) Powder bed immobilization with photopolymer, (4) Build volume reduction[59]	13
2.9	Drop spacing and common modes	14
2.10	Drop-Powder interaction analysis: (A) Influence of droplet on powder bed, and (B) Schematics of three granule formation mechanisms: (a) tunneling, (b) spreading, and (c) crater formation [71, 72, 73]	15
2.11	The categorization of three pore types in sintered BJ 316L: Optical Microscopy (OM) image (a) and corresponding schematic representation (b).[85]	19
3.1	Microstructural morphology of 316L S.S Powder by SEM	21
3.2	TGA Testing equipment and sample piece	23
3.3	Furnace for debinding and sintering	24
3.4	Profile of Debinding and Sintering	24
3.5	Dimension Test Equipment	25
3.6	Calculation of Saturation Level	25
3.7	Density Test	26
4.1	Delamination of green parts before and after depowdering process	29
4.2	Edge samples exhibited more defects compared to central samples	29
4.3	Powder leakage at the edge of printing platform during printing process	30
4.4	Suboptimal binder line	31
4.5	Samples of the 2nd batch	32
4.6	The printing of dog-bone components	32
4.7	Powder leakage and cracks during the printing	33
4.8	Binder lines during the 2nd printing	33
4.9	The 3rd printing session	34
4.10	Small cups for packing density test and the final small cubic samples	34
4.11	TGA data of sample 4	36
4.12	TGA data and derivative of sample 4 mass variation	36
4.13	Samples sintered within different atmosphere	37
4.14	XRD result of 316L stainless steel samples sintered within Ar and vacuum	38
4.15	Microstructural morphology of green part ($<18\mu\text{m}$)	38
4.16	OM images of 3 samples under different sintering conditions	39
4.17	SEM analysis about different points of sample $<18\mu\text{m}$, sintered in Ar	40
4.18	SEM analysis within different areas of sample $<18\mu\text{m}$, sintered in Ar	41
4.19	SEM image of the selected area	42
4.20	Comparison of the indentations for the three samples	46
4.21	Relationship between different sintering atmosphere and hardness, grain size and relative density	47
4.22	Grain size measurement through Image J	47
4.23	Microstructure of samples within diferent sintering atmosphere	48
4.24	Compression test on complete cubic sample	49

4.25 Complete sample, N-compressed complete sample, X/Y-compressed half sample 1, X/Y-compressed half sample 2	49
B.1 As-sintered samples	62
B.2 Samples for characterization	63
C.3 Acquisition Condition	65

List of Tables

1.1	Characteristics of powder bed-based metal AM process	2
2.1	Chemical composition of 316L stainless steel powders (wt.%) [85]	17
2.2	Characteristics of the phenolic resin based binder [87]	18
3.1	Particle size distribution of 316L stainless steel powder (<18 μ m)	20
3.2	Parameters and relevant values for saturation level test	22
3.3	Data of packing bed density	22
3.4	Parameters of different waveforms for Metal Binder	23
3.5	Saturation level under 3P mode	23
3.6	Specifications of Artec Space Spider 3D Scanner	25
4.1	TGA testing data	35
4.2	Element analysis/Oxide at different points	40
4.3	Element analysis/Oxide within different areas	41
4.4	Density of samples (2 \times 2 \times 2 cm ³)	43
4.5	Density values from 5 studies	43
4.6	Theoretical values of mass, volume, and density of samples 6–9 with Rhino 8	43
4.7	Test for density distribution	44
4.8	The effect of wax application on density	44
4.9	Dimensional Measurement Results of Samples with Varying Sizes	45
4.10	Average hardness value of 3 samples (HV10)	45
4.11	Vicker hardness values from 5 studies	48
4.12	Sample dimension change ("*" means after compression test), unit: mm	49
A.1	Session 1: Chiron Machine (1 st printer)	61
A.2	Session 2: Type 2000 (2 nd printer)	61
A.3	Session 3: Reassembled Chiron Machine (3 rd printer)	61

Nomenclature

Abbreviations

Abbreviation	Definition
AM	Additive Manufacturing
PBF	Powder Bed Fusion
DED	Directed Energy Deposition
BJP	Binder Jet Printing
BJAM	Binder Jet Additive Manufacturing
SS 316L	316L Stainless Steel
PSD	Particle Size Distribution
SEM	Scanning Electron Microscopy
OM	Optical Microscopy
XRD	X-ray Diffraction
TGA	Thermogravimetric Analysis
ND	N-Direction (Perpendicular to the powder bed surface)
XD	X-Direction (Powder spreading direction in the XY-Plane)
YD	Y-Direction (Perpendicular to XD in the XY-Plane)

1

Introduction

The rapid advancement of social productivity and technological progress leads to the conflict between traditional manufacturing techniques and advanced design concepts. Traditional manufacturing struggles to adapt to the rapid iteration of modern markets, lacks the capability to produce complex geometries under limited budgets, and fails to meet the growing demand for customization. These challenges have constrained further progress in social productivity, giving rise to Additive Manufacturing (AM) technologies. AM enables the conversion of two-dimensional designs into three-dimensional physical models, quickly transforming computer-based concepts into tangible objects. AM has integrated disciplines such as computer science, mechanical engineering, control engineering, and materials science since its inception in the 1980s, and thus, it has been widely adopted in fields including aerospace, biomedical, and automotive sectors, positioning itself as a pivotal technology in the future of manufacturing[1, 2, 3, 4, 5].

The ASTM F42 Committee classifies AM technologies into seven categories: Binder Jetting (BJP), Direct Energy Deposition (DED), Material Extrusion, Material Jetting, Powder Bed Fusion (PBF), Sheet Lamination, and Vat Photopolymerization. Unlike traditional subtractive or formative manufacturing methods, AM employs a layer-by-layer approach to build components, facilitating the production of geometrically complex parts and supporting a wide range of materials, such as metals, ceramics, and polymers[6]. Additionally, AM holds considerable economic value, including material recycling, streamlined processes, reduced production line investments, and decreased tooling and labor costs[7].

The predominant feedstock forms for metal AM are powders and wires[8], with PBF, DED, and BJP being the primary powder-based metal AM techniques. Table 1.1 gives a direct comparison among these three AM techniques. PBF and DED utilize thermal energy, such as lasers or electron beams, to melt materials in an inert or vacuum environment. However, rapid heating and cooling rates in these processes make it difficult to control microstructure, often resulting in residual stresses that can cause part deformation and cracking[6, 9, 10, 11].

In contrast, the BJP process forms components at ambient temperatures, followed by debinding and sintering under uniform thermal conditions, which eliminates residual stresses. Therefore, BJP is considered more environmentally friendly and suitable for metals with high reflectivity, thermal conductivity, or low thermal stability. Furthermore, BJP does not require additional support structures, providing greater flexibility and economic benefits. It has thus been recognized as "one of the most promising and competitive AM processes". However, the final density of metal components produced by BJP is usually lower than those produced by powder metallurgy or other metal AM methods, which causes inferior mechanical properties and limits the application of BJP products. Therefore, addressing this challenge remains a major focus for its development[12, 13, 14].

Table 1.1: Characteristics of powder bed-based metal AM process [15]

Process	Advantages	Disadvantages
PBF	High Printing Precision High Component Density Good Final Mechanical Properties	High Cost High Residual Stress Time Consuming
DED	High Printing Precision High Component Density	High Cost High Residual Stress External Support Required Limited Materials Time Consuming
BJP	High Resolution Low Cost Large Parts Printing Fast Printing Process No External Support	Limited Materials Choice Low Component Density Post-Processing Maybe Required

The commonly used metallic materials for Binder Jet Additive Manufacturing (BJAM) include stainless steel, nickel-based superalloys, titanium alloys, copper, and other metals. Among these, ferrous alloys (e.g., iron and steel) are widely employed in the aerospace, medical, automotive, and construction sectors, making them some of the most extensively applied and relatively mature materials for BJP technology. Achieving high-density stainless steel parts remains a critical research focus within BJP. Common approaches include infiltrating with a low-melting-point metal or using alternative methods such as nanoparticle jetting or the addition of sintering aids[16, 17]. Studies have also demonstrated that the density of parts produced using solely ferrous powders can be improved by optimizing parameters such as stainless steel powder particle size and shape, sintering temperature, and time[18]. The latter approach serves as the motivation for this project, which aims to enhance the density and industrial performance of products by optimizing printing and post-processing parameters using only 316L stainless steel powder.

This research opportunity is provided by the company CONCR3DE. One of CONCR3DE's core activities is the customization of material and application requirements, utilizing a diverse range of materials, including stone, ceramics, (bio)polymers, and stainless steel. To ensure that product quality can meet client expectations, this project aims to investigate how Binder Jetting Printing (BJP) can be used to achieve 316L stainless steel samples with desirable engineering properties. Since the engineering performance of the final samples is positively correlated with their densification, achieving high final density is crucial. Furthermore, in alignment with the company's resource allocation and production strategy, this project exclusively involves 316L stainless steel powder rather than mixed powders, and will use only the proprietary binder developed by the company.

1.1. Study Objectives

In this study, samples were fabricated using 316L stainless steel powder combined with a binder through a binder jet 3D printer. The materials and equipment employed in this project were provided by Concr3de. The primary objective of the study is to characterize the performance of the fabricated samples and identify effective approaches to enhance their properties based on experimental data. Accordingly, the project is divided into three specific objectives:

1. Determination of optimal green body printing parameters

Parameters such as powder packing density, layer thickness, and printing speed during the fabrication process significantly influence the properties of the green parts, including density, shape accuracy, and binder distribution uniformity. Therefore, identifying appropriate printing parameters is critical for the preliminary control of sample performance.

2. Optimization of debinding and sintering parameters

Both the debinding process and the post-treatment stage have a substantial impact on the

performance of metal samples produced via binder jetting. While the debinding process determines the residual binder content in the samples, the sintering process governs the microstructure of the samples, thereby affecting their engineering properties. In this project, sintering was selected as the post-treatment method.

3. Investigating the relationship between process parameters and final sample performance

The final engineering properties of the samples, such as hardness and tensile/compressive strength, are positively correlated with the ultimate density of the 316L stainless steel samples. Since the final density is influenced by the sintering and printing processes, understanding the specific effects of these parameters on the sample properties is of paramount importance.

1.2. Project Limitations

This project is rooted in the company's operational needs rather than pure academic research, which introduces the following constraints:

1. Resource limitations may affect results

Due to resource constraints within the company, practical challenges such as the use of two different types of 316L stainless steel powder, reliance on varied printing equipment, and potential machine malfunctions were encountered during the project. Additionally, given the time restrictions, the conclusions drawn from this study may not represent definitive results, and the parameters identified may not be optimal.

2. Incomplete experimental design

Since all resources were provided by the company, certain experiments were simplified or omitted. For instance, the debinding process was simplified due to the proprietary nature of the binder used by the company. Limited TGA testing was conducted to determine relatively optimal debinding parameters rather than conducting in-depth research. Similarly, tensile testing could not be performed because dog-bone-shaped samples could not be fabricated successfully, and compression tests were limited by the large size of the printed samples, which precluded repeated trials to validate findings. Furthermore, variations in powder and printing equipment contributed to considerable uncertainty in the sample density results.

3. Limited generalizability of conclusions

Since this project is based on Concr3de's specific production processes, the findings are heavily influenced by experimental equipment, raw materials, and environmental factors, and may not be applicable to other studies. For example, the printing process was conducted near a harbor, but the effect of humidity on 316L stainless steel powder was not considered, despite its potential to cause corrosion during sample storage. Additionally, the binder used in this study is proprietary, and its exact composition is confidential, making it difficult to evaluate its effect on the final properties of the 316L stainless steel samples. Consequently, the curing and debinding parameters determined in this study may lack broader applicability.

1.3. Thesis Structure

This thesis is structured into five main parts: the literature review, the methodology, the results, the discussion, and the conclusion.

- **Literature Background (Chapter 2):**

This chapter provides an overview of the technical background and fundamental principles of binder jetting (BJ) technology. It also discusses the technical specifics and advancements in BJ technology for stainless steel printing, with a particular focus on the challenges associated with printing 316L stainless steel using this method.

- **Methodology (Chapter 3):**

This chapter details the methods and equipment employed in the study, explaining their relevance to the research objectives and how they support the experimental process.

- **Results and Discussion(Chapter 4):**
This chapter presents the data and visual outcomes obtained from the experiments conducted during the study, analyzes these experimental results presented, and explore the underlying causes of observed phenomena and identifying potential optimization strategies.
- **Conclusion (Chapter 5):**
This chapter summarizes the key findings derived from the study. Additionally, it addresses the limitations of the research, offers recommendations for future work, and highlights existing research gaps.
- **Knowledge Gap and Future Research(Chapter 6):**
This chapter mentions the knowledge gap and relative research that requires to be done in the future.

2

Literature Background

Binder jet 3D printing (BJP) was first introduced by Sachs[19] in 1990. As an additive manufacturing (AM) technology, BJP involves the layer-by-layer bonding of powder materials using a binder to form green parts, which are subsequently processed through debinding and sintering to yield the final components. Numerous factors during the initial powder preparation, the intermediate green part printing, and the final sintering stages can significantly influence the performance of the final parts. This study aims to address these factors by fabricating 316L stainless steel samples using materials and equipment provided by Concr3de. The research focuses on characterizing the effects of various process parameters on the properties of the final components, such as density, hardness, and compressive strength, and identifying key parameters suitable for production optimization.

This chapter begins by outlining the development of BJP technology, followed by an introduction to its fundamental principles. It then discusses the outcomes and challenges associated with the production of 316L stainless steel samples via BJP, as well as the parameters that impact the performance of BJP-fabricated 316L stainless steel components. In summary, this chapter provides a preliminary overview of the foundational principles and critical parameters of BJP based on current research findings.

2.1. Development of Binder Jet Printing

Binder jet printing process was originally known as "3D Printing" or "ProMetal" technology[20, 21]. In 2013, the ASTM committee formally reclassified this process as "Binder Jetting Printing"[22]. This technique involves selectively bonding metal powder particles using a liquid binder to fabricate printed green parts. These green parts subsequently undergo post-processing steps, including debinding, sintering, and infiltration, to achieve the desired structural integrity, density, and mechanical performance. The binder jetting process primarily defines the component's geometry, while the subsequent post-processing steps enhance its densification and mechanical properties, as illustrated in Figure 2.1[23].

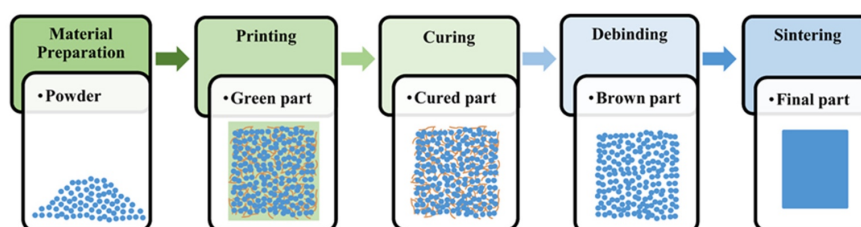


Figure 2.1: Process flow of binder jetting printing[23]

After Sachs and his team initially proposed the Binder Jetting (BJP) technology, the American company Z Corporation obtained the licensing rights to the technology in 1995 and subsequently launched

a series of printing devices. In 1996, the American company Extrude Hone acquired MIT's patent for the technology and introduced the world's first metal Binder Jet Additive Manufacturing (BJAM) machine, the ProMetal RTS-300, in 1997. In 2003, ExOne was established as a spin-off from Extrude Hone, focusing specifically on binder jetting for stainless steel components and casting molds. In 2013, the ASTM committee in the United States officially named the binder jetting technology as BJAM. In 2015, Z Corporation introduced a full-color BJAM printer. By 2018, metal BJAM was recognized as one of the "Top 10 Breakthrough Technologies" by MIT Technology Review. In 2021, the American companies Desktop Metal and Uniformity Labs jointly developed a BJAM printer capable of producing fully dense 6061 aluminum alloy components. In recent years, BJAM has expanded its range of printable materials beyond iron-based alloys to include titanium alloys, high-temperature superalloys, and reactive metals such as aluminum and magnesium, significantly broadening its application domains[24]. The development of BJP technique is shown in Figure 2.2[24].

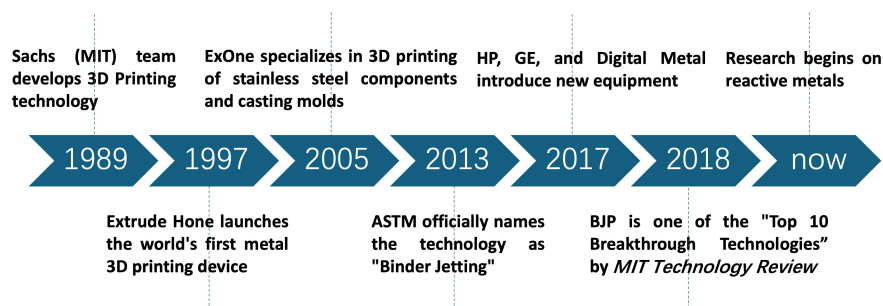


Figure 2.2: Development of BJP technique[24]

Compared to other additive manufacturing (AM) technologies, Binder Jetting Printing (BJP) offers several distinct advantages, including low cost, a wide range of compatible materials, good surface quality, and the absence of a need for support structures. Lindemann et al. investigated the cost structure of metal AM processes and concluded that machine costs contribute most significantly to the lifecycle cost of parts[25]. Unlike laser-based AM technologies, BJP does not require lasers or precision optical components, resulting in lower machine production costs. Additionally, BJP supports a broader range of materials compared to other AM techniques.

2.2. Printing Process

As described at the start of chapter 2, BJP is a rapid prototyping technology based on the discrete-stacking principle. The printer appearance is shown in Figure 2.3 [26], and the whole process containing both printing and post-processing is given in 2.4[27]. For a typical binder jet printer, there are two working platforms, namely powder supply platform (on the left) and powder building platform (on the right). And for a complete printing process, many steps are involved. First, the digital model of the final components will be designed and sliced into layers of the desired thickness within specific software. Next, the spreading roller will spread a layer of powder from the the supply platform to the building platform. Then, the printhead deposits the binder onto the powder bed selectively following the two-dimensional cross-sectional contour of the desired object. Through the infiltration of the binder among powder particles, the binder bonds with the powder within the selected region, undergoing physical or chemical reactions, while the remaining areas of the powder bed remain loosely packed. After the bonding within one powder layer, the building platform descends by one layer thickness, and

the powder bed ascends accordingly. Then, the roller will spread the powder again to fill the empty space created by the descent of the building platform, and printhead will give binder again. So with powder spreading, the next layer of powder will be bonded and formed. This cycle continues iteratively until all the required layers have been printed. Finally, the final product, also called green part, will be obtained. To make these components can satisfy the engineering requirements, post-processing is usually necessary.

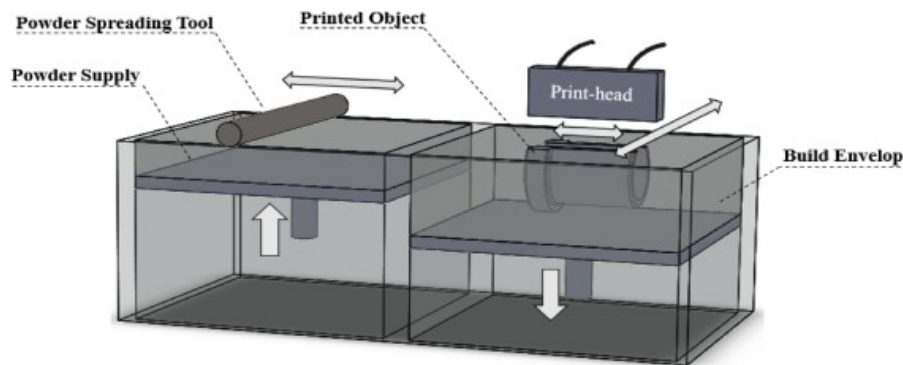


Figure 2.3: Schematic diagram of binder jetting system[26]

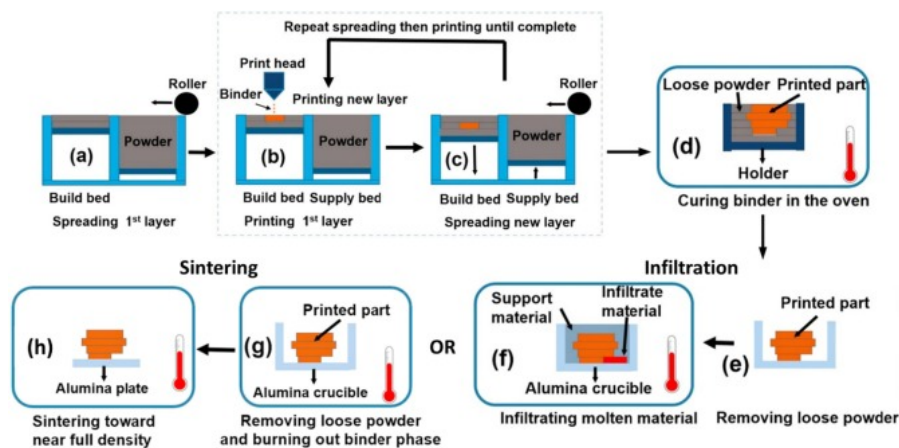


Figure 2.4: Steps of sample production by BJP[27]

2.2.1. Powder Preparation

Before the process illustrated in Figure 2.5 begins, an additional step is required: the preparation of powder materials. During this phase, selected powders undergo pre-processing operations such as drying and sieving to ensure uniform dispersion during the printing process. Research on various powder types, including different compositions and particle size distributions, led to the first application of ceramics in BJP in 1993. Components fabricated using this process consistently achieved densities exceeding 99.2% after sintering[28]. Notable ceramics produced through this method include alumina, silica, and titanium dioxide[29].

However, early studies highlighted that fine powders, which are necessary to achieve optimal powder bed density, often exhibit poor flowability, hindering the formation of defect-free layers[28]. Additionally, green bodies produced using dry powders typically have relatively low density, necessitating additional steps such as isostatic pressing to improve density. These supplementary steps significantly constrained

the range of geometric shapes that could be effectively processed. Consequently, certain material preparation techniques have been developed to enhance the performance of final components.

For instance, in the manufacturing of metallic and ceramic materials, polymer binders are applied to produce green components, which remain in an unsintered or pre-fired state. After production, these green parts are removed from the additive manufacturing system and subjected to 2–3 furnace cycles. During the initial cycle, a low temperature is applied for several hours to remove the polymer binder. In the second cycle, high temperatures are used to sinter metal or ceramic particles, resulting in a component density of approximately 60%. The third cycle introduces a bronze ingot (or an alloy with a lower melting point than the powder alloy) into the furnace, facilitating the infiltration of bronze into the part's pores and achieving a final density exceeding 90%. This furnace-based process is consistent with the indirect processing methods used for producing metallic and ceramic components, as illustrated in 2.5 [30].

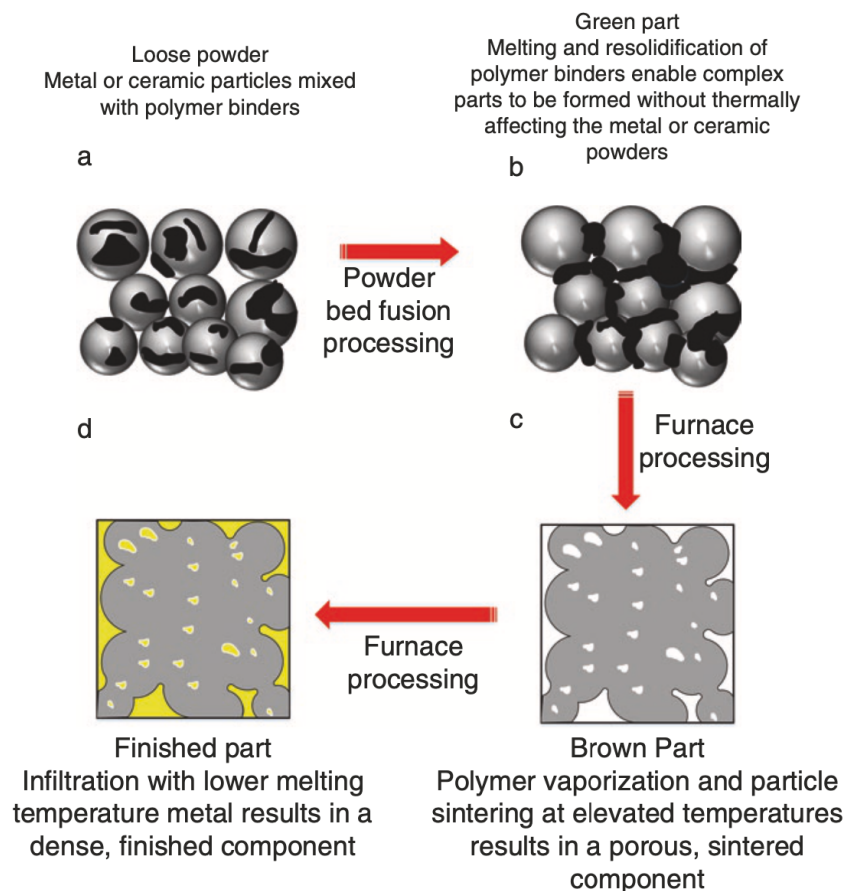


Figure 2.5: Indirect processing of metal and ceramic powders using PBF[30]

This indirect processing method uses polymer-coated metallic powders or a mixture of metallic and polymer powders to create metallic components. The process consists of two main stages: debinding and infiltration/consolidation. During the debinding stage, the polymer binder is removed from the green part through melting and evaporation, while elevated temperatures promote slight necking (sintering) between metallic particles. Subsequently, a lower-melting-point metal is introduced to fill the remaining porosity, resulting in a fully dense metallic part. The consolidation stage involves additional sintering and densification to reduce porosity. Infiltration offers excellent dimensional control with minimal shrinkage; however, the resulting structures are composites, unlike monolithic structures

formed from a single material type[30].

Furthermore, the addition of auxiliary components can optimize powder performance. For example, incorporating low-melting-point additives as sintering aids into stainless steel powders can reduce production costs while enhancing the density and mechanical properties of the final components. A. Sharon et al. [sharon1997environmental] blended copper-based powders with 304L stainless steel powders, utilizing the transient liquid phase to improve the sintered specimens' density and corrosion resistance. Specimen porosity was observed to be 6.5% when the copper additive content was reduced to 7 wt%. Do et al. [31] explored the effects of boron-based additives (B_4C , BN, B) on the density and mechanical properties of sintered specimens. Their study involved sintering specimens with varying sintering aid contents for 6 hours in an argon atmosphere. The addition of 0.75 wt% B_4C at 1200°C achieved a relative density of 99.67% without significant deformation. Furthermore, Abenojar et al. [32] incorporated 1.5 vol.% and 3 vol.% SiC powder into 316L stainless steel. The reaction between SiC and the stainless steel matrix produced a low-melting Fe-SiC phase, which enhanced both the density and mechanical properties of the sintered bodies. At 3 vol.% SiC content, the sintered specimens exhibited optimal wear resistance, although there was a slight reduction in corrosion resistance.

2.2.2. Curing and depowdering

After printing, the binder must be dried to impart sufficient green strength to the printed powder[27]. This curing process involves removing the build box from the printer, subjecting it to heat to ensure the binder is adequately dried, and enabling the manual extraction of green parts from the powder bed. Typically, the build box containing the powder bed and printed parts is transferred to an oven, where the curing temperature ranges from 180 to 200°C, with the duration determined by the build box volume and binder properties [33]. Watters et al. [34] proposed an enhanced curing protocol incorporating vacuum, heat, visible light, and pressure to improve the strength of binder jet 3D printed components. Following the curing process, the green parts achieve sufficient strength for handling and are subsequently transferred to the densification furnace. During this stage, loose powder in the build box is removed through a combination of vacuuming and careful manual brushing by operators. Individual components are further cleaned using brushes for surface finishing or gentle vacuuming/air blasting to clean intricate internal features. Special care is required for printed parts with delicate features or overhanging structures to prevent breakage. The green parts, consisting of metal powder loosely bound by the binder, are then densified through sintering or infiltration to achieve high density and the desired mechanical properties[27].

2.3. Post Processing

After printing, the green body, which is enveloped by unbound powder, requires post-processing to transform into a product. Post-processing includes debinding and sintering, and for binder jet process, infiltration can be applied for a high densification during sintering[23, 35].

2.3.1. Debinding

Most binders are based on organic compounds that decompose when heated. Thus, debinding step affects both densification and residue's composition. For BJP, thermal debinding parameters are determined through thermogravimetric analysis of the dried binder in the sintering atmosphere to identify critical decomposition temperatures. Heating at these key decomposition temperature points may be adjusted to ensure complete binder removal without generating excessive gas pressure within the pores. Gas transport and part heating can be slow, especially when parts are surrounded by refractory powder for support during sintering. Wu et al.[36] demonstrated that vacuum debinding of alumina-loaded slurry achieved higher density in a shorter processing time than thermal debinding at atmospheric pressure. The impact on composition may depend on particle size and the surrounding atmosphere. Smaller particles are more likely to absorb carbon due to increased surface area. In some

cases, oxidizing atmospheres may be used to improve binder removal, while reducing atmospheres is necessary for most metals' optimal sintering. The debinding process produces a 'brown' part, which is more fragile than the green part due to the significant removal of the binder system, and the duration of the process depends on the geometry of the part and the thickness of the section. Besides, the composition and resulting properties of brown part can be sensitive to the atmospheric composition during post-processing[26, 35].

2.3.2. Sintering

Oxidation reactions and residual binder can lead to the formation of unintended compositions. As a result, debinding and sintering are typically performed concurrently in a protective atmosphere, such as argon, or under vacuum conditions. Sintering mechanisms can be categorized into two types: non-densifying and densifying. At lower temperatures, sintering is primarily governed by non-densifying mechanisms, such as surface diffusion, lattice (volume) diffusion on particle surfaces, and vapor transport. During this stage, while particle coarsening occurs, neck growth remains minimal. As the temperature increases, densifying mechanisms become dominant. For metallic materials, grain boundary diffusion and lattice diffusion between particles are the primary densifying mechanisms. These processes facilitate neck growth, which significantly enhances the densification of the component[23, 37].

Figure 2.6 illustrates the three stages of the sintering process. (a) represents the initial metallic bond formed at particle contacts due to atomic diffusion at lower sintering temperatures; (b) and (c) represent the formation of sintering necks as atomic migration from the powder particle surfaces to neighboring particles occurs with increasing sintering temperature and also shows the ongoing growth of sintering necks, gradual reduction in pore size and serialization as the sintering temperature increases and the holding time extends[38].

The initial stage primarily involves the formation of sintering necks between particles, where pores remain interconnected without significant grain growth. Only about 2-3% densification occurs during this initial stage. The intermediate stage occurs at slightly higher temperatures and involves the evolution of microstructures at interconnected pores. Sintering necks grow from approximately 30% of particle diameter to about 50%, significant enough to allow interference and overlap. Grain growth and pore shrinkage primarily occur through particle rearrangement[39]. Up to 93% densification occurs during the intermediate stage[40]. The final sintering stage occurs at temperatures similar to or slightly higher than the intermediate stage and primarily involves the closure of spherical pores. In this stage, pores move along grain boundaries or become isolated within grains. While the density of the sintered body slightly increases, grain growth also occurs rapidly. If the sintered body cannot achieve complete densification, pore coarsening may occur [41].

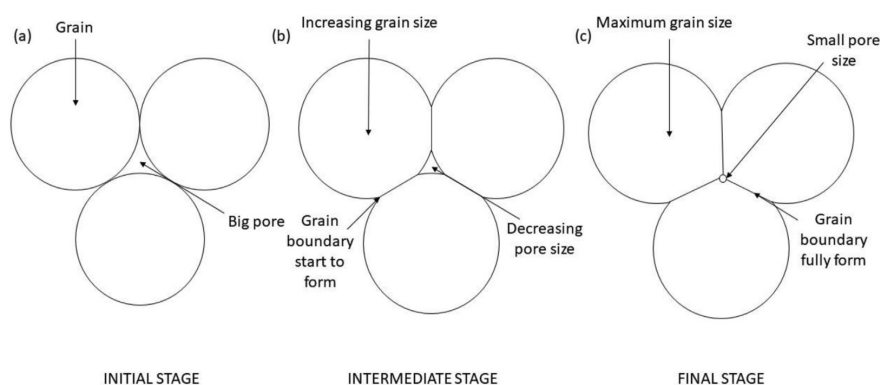


Figure 2.6: Sintering model[38]

During the sintering process, the components are subjected to heat, and mass transport, primarily through diffusion, reduces surface free energy and decrease pore fraction within the compact. Smaller particles enhance the sintering capability of the compact due to their higher surface energy[42, 43]. Particle morphology also has an impact on sintering behavior[44]. Furthermore, the shape of the powders determines how they are packed in the green state, consequently affecting the density of the sintered final product[45]. According to the research of Mohsen Ziaee et al.[26], sintering can achieve almost complete density (> 99% of theoretical) when the green body is highly dense, typically necessitating a green density exceeding 50%. Lower densities result in pore enlargement with limited densification. Shrinkage will occur during sintering densification, typically ranging from 15% to 20%, depending on green part density.

Additional steps are required when sintering alone cannot achieve desired densification. The choice of techniques depends on whether the porosity is interconnected or closed. In cases of open porosity, infiltration with low-melting-point alloys can be highly employed. For closed porosity, hot isostatic processing (HIP) can significantly reduce or eliminate pores to enhance final properties[46]. Typically, sintering must attain a 90–92% density to create discrete circular pores suitable for hot isostatic pressing[26].

2.4. Important Parameters

2.4.1. Powder Related Parameters

Particle Size Distribution

The particle size distribution (PSD) of powder influences the flowability and deposition of parts after sintering, determining the powder packing ratio, binder saturation in the green state, and final part surface roughness, and also impacts on layer thickness[47]. Changes in particle size distribution and average size can alter powder bed packing density and flowability during printing. They also affect the powder bed's pore size distribution and uniformity, subsequently influencing binder spreading and the strength of printed parts[48].

Particle size distribution and average size can affect the maximum packing density of the powder bed, thus impacting the composition and properties of the final parts[49]. Broader particle size distributions are associated with higher packing densities, as smaller particles fill the gaps between larger ones, thereby increasing packing density[50]. For powders with narrower size distributions, no matter fine or coarse particles may create voids during binder jetting that cannot be eliminated in the final sintering stage. While printing with fine powders can enhance the volume density and surface roughness of sintered parts, their limited flowability and poor filling performance make them less commonly used as direct printing materials[51]. A full particle size distribution can provide higher green density, reduce the generation of pores and thereby enable higher density in parts after sintering[52]. Typically, multimodal powders can help to improve powder bed packing density, with coarse particles ensuring flowability. In contrast, fine particles fill the gaps between larger ones to enhance powder bed packing density[31]. So a proper particle size distribution is advantageous for solidifying the powder during printing, improving the final part surface roughness, and reducing dimensional deformation and shrinkage.

In the case of binder jet, the powder remains packed on the powder bed, so the bulk density determines the green part density, which determines the sintering performance of the subsequent powder compact. The powder size in BJ ranges from 0.2 to 200 μm [53]. Figure 2.7 [54] qualitatively displays micrographs of various BJP-manufactured metal powder particle sizes, ranging from fine to coarse. Compared with larger particles, finer particles exhibit poorer flowability due to inter-particle friction that inhibits particle sliding and effective packing. Thus, attributed to greater van der Waals forces, small particles

own larger surface area and high inter-particle friction, and hence, the lower flowability and suboptimal packing properties[20, 47] are caused.

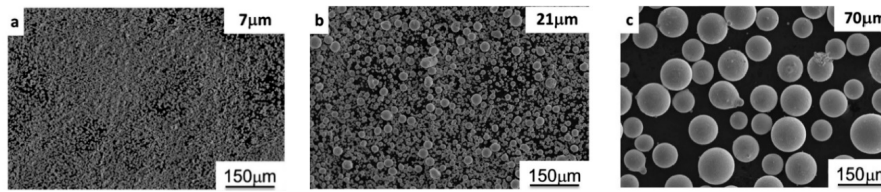


Figure 2.7: Micrographs of gas-atomized Inconel 718 powders (a) 7 μ m, (b) 21 μ m, (c) 70 μ m[54]

Packing Density

Powder spreading is a crucial step in powder bed additive manufacturing, significantly impacting powder bed quality, primarily in terms of density and surface condition. Key factors influencing powder spreading include feedstock powder characteristics, such as particle size and morphology, and the type of spreader employed (e.g., wiper, counter-rotating roller, forward-rotating roller). Additionally, methods involving multiple layers or a single layer for assessing powder bed density can lead to divergent results.

According to the research of Y. Bai et al. [55, 56], compared with monodisperse powder, the mixture of bimodal powder exhibits higher packing density (8.2%), better flowability, increased sintered density (4.0%), and reduced body shrinkage during sintering (6.4%). Moreover, spherical morphology is the favored choice considering both the flow ability and the compatibility with binders of powder materials during the recoating step. Larger powder particles offer enhanced flow and packing quality but a reduced sintering driving force which potentially tends to hinder densification during sintering. The phenomenon that most powder mixtures display an extended particle size deviation rather than a discrete bimodal distribution can be attributed to the inadequate large-to-small particle size ratio employed in the research conducted by Bai et al. [55]

Multiple modes in feedstock materials significantly influence various properties of the final binder jetted components [57]. The research by Do et al. [31] indicates a notable rise in packing density, from 51.3% in unimodal PSDs to 60.3% in bimodal PSDs and further to 63.9% in trimodal PSDs, thereby enhancing the surface quality of the binder jetted SS316L stainless steel. Mirzababaei et al. [47] presented findings where a bimodal powder sample with a 70D-30S ratio demonstrated a green density of 60.3%. Additionally, Sohn et al. [58] reported that the extension of particle size distribution contributed to an increase in packing density, with Gaussian and log-normal size distributions of bimodal powders with a 60:40 ratio yielding packing densities of 78.2% and 77.5%, respectively [47].

There are many methods to measure the powder bed density. A straightforward method is to measure the total mass and bulk volume of the entire powder bed consisting of multiple powder layers. Alternatively, powder bed density can be estimated by measuring the mass and bulk volume of a portion of the powder bed. Cups and fences can be printed within the powder bed, as shown in Fig 2.8 (a) [59], then the enclosed powder in cups or fences can be collected for density calculation. This method is also used for single-layer bed density measurement by printing fences matching the layer thickness [60]. There are other methods for local powder density measurement. For instance, cylindrical or square tubes can be inserted into an established powder bed from above (Fig 2.8 (b)), and the powder within them can be gathered [42, 61]. Besides physical tools, a portion of the powder bed becomes immobilized by applying liquid photopolymer resin to a specific area of the powder bed and curing it with light. Using computed tomography (CT) scanning on the immobilized powder bed and employing image processing software, powder bed density can be calculated (Fig. 2.8 (b)) [62]. It is also possible to simplify powder bed density measurement by reducing the build volume (Fig 2.8 (d)) [63, 64].

In addition to experimental methods, powder bed density has been investigated using Discrete Element Method (DEM) simulations. DEM tracks the motion of individual particles by solving Newton's

equations for both translational and rotational motion, allowing for the calculation of powder bed density based on particle locations[65].

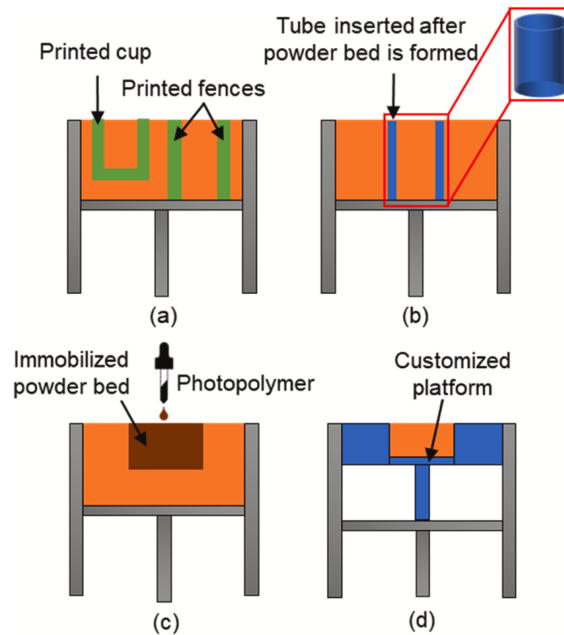


Figure 2.8: Measurement of powder bed density: (a) Cups/Fences printing, (b) Tubes insertion, (c) Powder bed immobilization with photopolymer, (d) Build volume reduction[59]

Flowability

Powder flowability denotes the powder's movement ability during printing, which is pivotal in binder jetting. It governs the powder's consistent deposition onto the powder bed. Favorable flowability leads to uniform powder spreading, enhancing the final part's resolution, dimensional accuracy, and density. Inadequate flowability causes uneven powder bed surfaces, potentially resulting in part defects and performance issues [49]. Flowability relies on several parameters: powder morphology, average size, size distribution, composition, and external environmental factors [27]. Typically, spherical powders demonstrate superior packing density, facilitating improved flow and settling, while irregular powders exhibit poor flowability due to inter-particle adhesion. Studies by the Chmielus team comparing different powder morphologies revealed that spherical powders with lower oxygen content yield final parts with higher relative density and superior mechanical properties compared to irregular powders [66]. Decreasing particle size in fine powders enhances van der Waals forces between particles, notably diminishing powder flowability by overcoming gravitational forces [49, 48]. Thus, particle size emerges as a crucial factor influencing powder flowability. Furthermore, adjustments in external environmental parameters, such as humidity, temperature, and additives, can also alter powder flowability.

2.4.2. Printing Process Parameters

Droplet Spacing and Line Spacing

The deposition of binder droplets onto the powder bed is governed by factors such as print head velocity, the diffusion rate of the binder within the powder layer, droplet spacing (d_1), and line spacing (d_2), as shown in Figure 2.9a[26, 27]. Upon deposition, the binder droplets infiltrate the powder bed under the influence of capillary forces and gravity until equilibrium is achieved. When droplet spacing is large, individual droplets are deposited independently and subsequently absorbed. As spacing decreases, overlapping droplets create narrower, fan-shaped lines. A further reduction in spacing eliminates the

fan-shaped geometry, producing smooth and straight lines with uniform edges, which represent the narrowest lines achievable during printing. However, excessive reductions in spacing may result in localized line expansion, leading to non-uniform widths. At elevated powder bed temperatures, where evaporation rates exceed the ejection speed of droplets, the droplets dry individually, rendering spacing irrelevant to line width [67].

Reducing the spacing between droplets increases binder consumption, which enhances the strength of green parts but can lead to broader binder lines, thereby compromising resolution [68, 69]. Excess binder can be removed post-printing through the application of heating elements, allowing for smaller spacing while maintaining high precision. Given that nozzle distances generally exceed line spacing, multiple injections are often required to complete a single layer. Alternatively, alternating droplet deposition can mitigate oversaturation but involves additional steps, thereby reducing production efficiency [26]. While excessively small line spacing prolongs print time and heightens the risk of oversaturation, overly large spacing may result in edge sealing, obstructing binder infiltration [27, 68]. Optimal spacing facilitates the rapid absorption of droplets, enabling adjacent lines to form a well-bonded powder layer.

Figure 2.9b illustrates four types of line defects. Only diagram (c) representing the ideal condition, while the other three result in diminished print accuracy. (a) depicts discrete droplet distributions when droplet spacing is large, preventing overlap, (b) shows the coalescence of droplets when the diffusion diameter of the droplets is marginally smaller than the spacing, and (d) illustrates instability caused by excessively small droplet spacing[70].

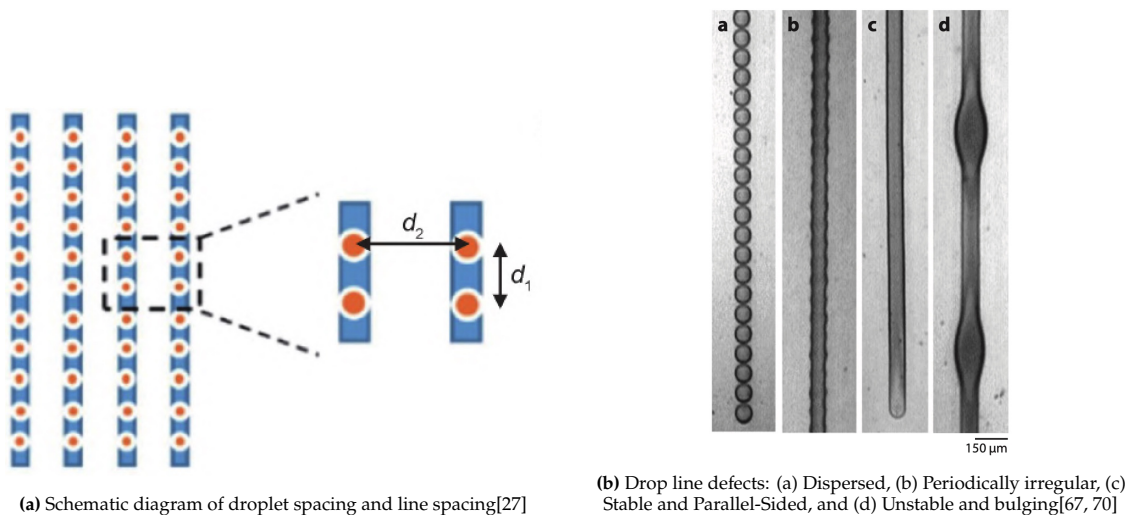


Figure 2.9: Drop spacing and common modes

Binder-Powder Interaction

The dimensional accuracy of BJ-printed parts is determined by the binder's deposition within the powder bed, making an optimal collision between the binder and the powder bed crucial [71]. Figure 2.10 (A) illustrates the effects of droplets on the powder bed, with (a) to (e) representing the powder bed's decreasing absorption capacity for the binder. The powder ejection observed in (b) and (c) is a primary cause of surface roughness in the samples[72]. Figure 2.10(B) presents three collision modes. In Figure 2.10 (B)-(a), a tunneling effect is observed in fine, viscous powders (similar to (A)-(b)), where the droplet penetrates the powder bed and pulls loose agglomerates, resulting in the formation of spherical particles due to incomplete penetration. (B)-(b) depicts the ideal collision effect, while (B)-(c) (similar to (A)-(c)) shows the formation of powder craters when droplets impact the dense powder bed at high speeds[73, 71].

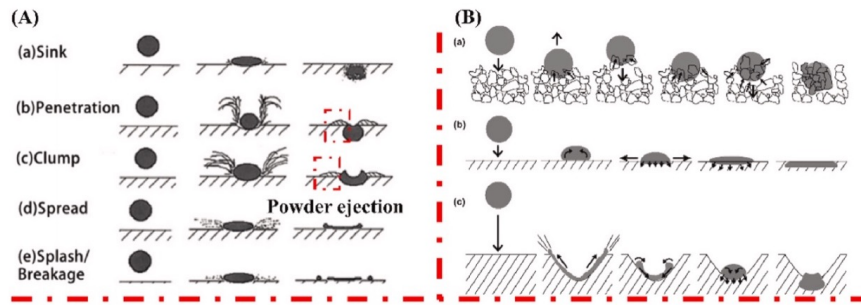


Figure 2.10: Drop-Powder interaction analysis: (A) Influence of droplet on powder bed, and (B) Schematics of three granule formation mechanisms: (a) tunneling, (b) spreading, and (c) crater formation [71, 72, 73]

The wetting of droplets depends on the relative sizes of liquid droplets and powder. It can be categorized into two cases: when liquid droplets are larger than the powder, it involves four stages—droplet formation, coalescence, adhesive migration, and mechanical dispersion; when liquid droplets are smaller, the liquid covers the powder and infiltrates through capillary pressure [26]. In practical printing, droplets impact the surface at high speeds, and their kinetic energy is comparable to the surface energy of the powder. Interactions between adjacent droplets can complicate wetting behavior. These issues can lead to printing defects such as aggregation, splattering, feathering, and leakage. To address these problems, adjustments to droplet printing patterns, wettability improvements, or smaller droplets to enhance penetration speed may be necessary [74].

Layer Thickness

Layer thickness refers to the height of the powder layer constructed along the Z-axis during the printing process, typically ranging from 0.0889 to 0.2286 mm [48]. The choice of layer thickness is generally based on the powder's particle size, with the minimum layer thickness being larger than the diameter of the largest particles and preferably around three times the size of the powder particles [56, 49].

A study conducted by the Salarian team [75] involved printing pure iron (Fe) powder with three different layer thicknesses (75, 100 and 125 μm). The research indicated that when binder saturation is consistent, increasing the layer thickness can result in inadequate binder penetration into the current powder layer, leading to incomplete bonding of the unpenetrated powder. And this phenomenon leads to the disintegration of the green part. Increasing both layer thickness and binder saturation may not significantly differ in terms of printed part performance. However, increasing the layer thickness while keeping binder saturation unchanged may lead to decreased performance of the green part [76] and an increase in porosity [77]. Furthermore, when at optimal sintering parameters, reducing the layer thickness largely reduces the porosity of the sintered part [77, 78].

Binder Saturation

The build bed is filled with powder, voids or air, and binder during the printing process. The volume fraction of the build binder is referred to as the binder saturation, and it can be defined by equation 2.1 [47, 49]:

$$P_s = \frac{V_{\text{binder}}}{V_{\text{air}}} \quad (2.1)$$

In this equation, P_s represents the binder saturation, V_{binder} is the volume of binder injected per layer, and V_{air} is the volume of voids within the powder bed.

Saturation is commonly used to describe the quantity of binder, indicating printing stability [47]. Binder

saturation depends on factors such as the wettability of the powder and binder, powder shape, size distribution, and bulk density[79]. The choice of saturation level needs to be made properly because it affects the printing quality and the final sintering density[56]. Inappropriate binder saturation (either too high or too low) can result in uneven distribution of the powder layers, significantly impacting surface roughness and causing inaccuracies in part dimensions[27].

When binder saturation is low, there is insufficient binder binding between powder particles, leading to powder detachment from the green part and inadequate surface finish. Additionally, the weak bonding between powder particles and layers due to insufficient binder can reduce the green part's mechanical strength[80]. On the other hand, when binder saturation is too high, excessive powder is bound to the surface of the green part, causing surface expansion and affecting the geometric shape of the part. Moreover, the excessive binder may seep out of the part's boundaries, resulting in reduced dimensional accuracy[79].

Yang et al. [80] conducted a study investigating the influence of binder saturation on the dimensional accuracy of Ti-6Al-4V and stainless steel 420 green parts. The result indicates that under specific conditions and with a consistent powder layer thickness, the strength of green parts tends to increase as the saturation levels rise [76]. However, excessive binder saturation led to collapse within the parts, causing inadequate dimensional accuracy. Moreover, as the binder content increased, the degree of collapse gradually intensified [81]. .

Curing Temperature

Once all the layers are completed, an additional process, namely curing, will be done to enhance the strength of the green body before other processing. Depending on the nature of the binder used, green parts are typically heated and maintained at temperatures between 180 to 200 °C for a specific period to cure them[27]. Through further polymerization of organic binder and cross-linking of dried solvents polymer, the structural integrity of the parts can be improved[47].

2.4.3. Post-Processing Parameters

Debinding Temperature

As mentioned at the start in Section 2.3, debinding and sintering are involved within post-processing. Debinding is the initial stage of sintering, where the green parts are heated within a specific temperature range, causing the binder to become unstable and decompose into easily evaporable components. Thus, a key factor here is the temperature. Standard debinding methods include thermal debinding, catalytic debinding and solvent debinding, etc.[26]. Most binders melt below 150 °C but may only completely evaporate once temperatures reach 300 to 500 °C[47].

The debinding process is crucial for sintering setting up and can significantly impacts the final part's performance, accuracy, and consistency. If the binder is not entirely removed, residual carbon elements may diffuse into the interior of the part, affecting its properties. Once the binder has been adequately removed, the green parts are transferred to a sintering or infiltration furnace to enhance the density and performance of the parts.

Sintering Parameters

Sintering density and shrinkage are typically used to evaluate the sintering effect, and the parameters that can affect the final component's properties include temperature, heating rate, dwelling time, atmosphere, etc. Research has shown[82, 83] that as the sintering temperature increases, the mechanical properties and density of the final part also increase. However, when the temperature exceeds the optimal sintering temperature, the growth of grains is followed by an increase in porosity, which leads

to a gradual decrease in mechanical performance.

A study by Miyanaji's team[51] investigated the impact of different sintering temperatures and heating rates on sample properties. The research indicated that the increase in heating rate leads to a decrease in final density but an increase in densification speed. The variation of sintering temperature has little impact on final part density because the lower heating rates stimulate pores closure within printed parts before sintering, so the peak sintering temperature has less influence on density. And Enneti's team[33] employed two different sintering methods (vacuum sintering and pressure sintering) for WC-12% (mass fraction) cobalt green parts. Their results showed that sintered samples under pressure exhibited superior density and performance than those within vacuum. Increasing the sintering temperature with constant pressure holding time can significantly improve density and shrinkage. Similarly, increasing pressure holding time at constant sintering temperature resulted in an increased density and reduced shrinkage.

In addition to the basic sintering, various techniques can be employed to obtain the desired metal components. These techniques, including hot isostatic pressing, annealing, aging treatment, mechanical grinding, and others, serve to improve the performance and density of sintered parts[46, 78].

2.5. 316L Stainless Steel and BJP

Metal Binder Jetting (MBJ) technology demonstrates significant potential in reducing manufacturing costs and lead times for complex geometries and designs compared to traditional manufacturing methods[84]. One of the most commonly used alloys in numerous industries is 316L stainless steel, the chemical composition of which can be found in Table 2.1. Due to its excellent formability, outstanding biocompatibility, and superior corrosion resistance, SS 316L austenitic stainless steel is a highly favored material in biomedical, aerospace, and automotive industries[85]. In the context of Metal Binder Jetting technology, SS 316L is also a popular material choice, with extensive research on its properties. Studies have approached MBJ from various perspectives, including powder characteristics, binder formulation, and post-treatment process[86].

Table 2.1: Chemical composition of 316L stainless steel powders (wt.%) [85]

wt.%	Fe	Cr	Ni	Mo	Mn	Si	C	O
Standard alloy 316L	Bal.	16-18	10-14	2-3	<2	<1	<0.03	/
Provided by manufacturer	Bal.	17.92	12.03	2.42	0.051	0.51	0.009	0.0466

For instance, Truong Do et al.[31] applied mixing 316L stainless steel powders of different grain sizes and adding boron-based powders as sintering aids. They investigated the effects of sintering temperature and sintering aid concentration on the densification and mechanical properties of the printed green bodies. Another study by Yiwei Mao et al.[87] focused on creating high-strength 316L green parts with low binder saturation using a specially developed binder, examining the effects of binder saturation and layer thickness on the quality of the green parts. Additionally, research by Mao et al.[85] explored the impact of vacuum sintering temperature on the density, porosity, linear shrinkage, microstructure evolution, and tensile properties of sintered parts, along with the potential influences of different types of pores on the performance of sintered BJ 316L. Alberto Cabo Rios [88] and colleagues investigated the microstructural evolution of phases and porosity characteristics of 316L stainless steel produced through BJ technology.

In the binder jet processes, the green density of the parts typically ranges between 50% to 60%, necessitating sintering to enhance densification and thus improve overall mechanical properties[88, 86]. Microscopically, sintering involves the formation of sintering necks between powder particles, reducing interparticle gaps until they disappear. This process manifests macroscopically as a reduction in the dimensions of the sintered body in all directions[47]. The final properties of 316L stainless steel parts produced by MBJ largely depend on the sintering densification process. The main influencing factors of

Table 2.2: Characteristics of the phenolic resin based binder [87]

Viscosity $\mu(\text{mPa} \cdot \text{s})$	Surface tension $\gamma(\text{mN/m})$	Density $\rho(\text{g/cm}^3)$	Nozzle diameter $\sigma(\mu\text{m})$	1/ Oh
9.8	33.05	1.09	40	3.87

the final properties include material-related factors such as the chemical composition, size, and shape of the powder, and process-related thermodynamic factors like sintering temperature, heating and cooling rates, holding time, pressure, and protective atmosphere. These factors jointly determine the microstructure and properties of the sintered body.

Different AM techniques have varying impacts on 316L stainless steel. A study by Mengchen Xu[89] compared the microstructure and mechanical properties of components fabricated by LPBF and BJ. The research found that the grain size of LPBF samples was five times smaller than that of BJ samples, leading to a relative density of $99.20 \pm 0.30\%$ for LPBF samples compared to $96.54 \pm 0.54\%$ for BJ samples. The mechanical properties of LPBF samples were superior, with tensile strength and compressive yield strength of 669.92 ± 18.68 MPa and 75.65 ± 5.77 MPa, respectively, compared to 437.55 ± 10.11 MPa and 78.65 ± 3.57 MPa for BJ samples. Additionally, the extent of crack propagation was greater in BJ cells than in LPBF cells.

The post-treatment is always required for the binder jet processing process due to the high porosity of the green body. As shown in Figure 2.6, sintering leads to the grain growth and necking phenomenon. The research on BJ SS 316L at various sintering temperatures revealed that all samples exhibited an equiaxed austenitic microstructure, with the average grain size remaining below 30 micrometers. Grain growth was not significant at temperatures below 1360 °C; however, a substantial increase in grain size was observed when the sintering temperature exceeded this threshold[85]. The study conducted by Alberto Cabo Rios[88] examined the dilatometry results for both green and pre-sintered 316L stainless steel samples. The findings indicated distinct behaviors before the isothermal sintering phase. For example, the pre-sintered samples demonstrated notable thermal expansion, whereas the green samples underwent both shrinkage and expansion. This phenomenon might be attributed to the minor rearrangement of powder particles during the debinding process, with no marked shrinkage anisotropy noted at this stage. Additionally, a rapid increase in shrinkage rate was observed at sintering temperatures of 1370 °C, which is believed to be a result of the γ to δ phase transformation.

To investigate the impact of sintering temperature on the performance of final BJ SS 316L components, Mao et al. [85] who used self-made binder (data in Table 2.2) discovered that with the increase in sintering temperature from 1300 °C to 1380 °C, the material's porosity decreased and became more rounded, the grain size enlarged, and the mechanical properties progressively improved. Sintered parts achieved a favorable relative density of 92.0% and mechanical properties, with an ultimate tensile strength of up to 473.7 MPa and an elongation of up to 40.22% at a sintering temperature of 1380 °C. Moreover, they identified three types of pores in the sintered BJ 316L components (Figure 2.11):

- **Type I pores:** Small intra-grain pores formed due to faster grain boundary movement compared to pore migration, making them persistent during late-stage sintering and hindering densification.
- **Type II pores:** Grain boundary pores, smaller than grains, appearing in early to mid-stage sintering and fully removable during final-stage pressureless sintering.
- **Type III pores:** Large, irregular inter-grain pores, typically located between layers and aligned perpendicular to the printing direction, acting as stress concentration sites and significantly reducing mechanical properties. These are commonly observed in binder jetting.

It can be known that Type II pores can assist in reducing grain size, but both Type I and III pores hinder densification, with Type III posing a significantly greater challenge. So it is wise to try to avoid Type III pores in metal BJP.

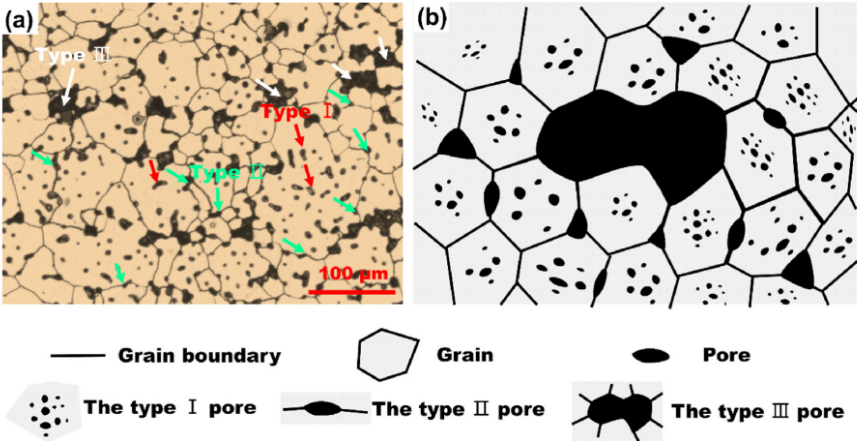


Figure 2.11: The categorization of three pore types in sintered BJ 316L: Optical Microscopy (OM) image (a) and corresponding schematic representation (b).[85]

To summary, although the various challenges encountered in BJP process, 316L stainless steel is still be favored in the industrial sector due to its superior mechanical properties. Additionally, recent studies show that binder jet technology has great potential for producing metal products.

3

Methodology

The overall experimental process centered on printing and sintering. As discussed earlier, the key steps in the sample preparation process were printing and sintering. Therefore, printing parameters needed to be continuously adjusted based on the results to improve print quality, while sintering required optimization based on TGA data to determine the appropriate sintering time and temperature for the 316L stainless steel samples. Subsequent measurements and characterizations were conducted to validate the engineering performance of the samples produced through printing and sintering.

The main objectives of the project are a) to optimize printing parameters in order to achieve a green part with high dimensional accuracy, b) to obtain a sample with high density through appropriate debinding and sintering processes, and c) to investigate the final sample's properties (such as density, hardness, and microstructure) to assist the company in establishing reliable printing parameters for 316L stainless steel samples.

3.1. Powder and Binder

Two types of 316L stainless steel powders are used in this experiment: one with a particle size of less than 18 micrometers, produced by Ampere in France, and the other with a particle size of less than 25 micrometers, produced by MatrixNano in India. However, only the particle size distribution (PSD) of Ampere's powder is available (Table 3.1), so this paper cannot provide the PSD data of MatrixNano's powder (<25 μm). Figure 3.1 shows the SEM images of both powders. The binder applied is provided by Concr3de, designed for metallic powders.

Table 3.1: Particle size distribution of 316L stainless steel powder (<18 μm)

	D10	D50	D90
Particle Size (μm)	5.3	12.3	21.6

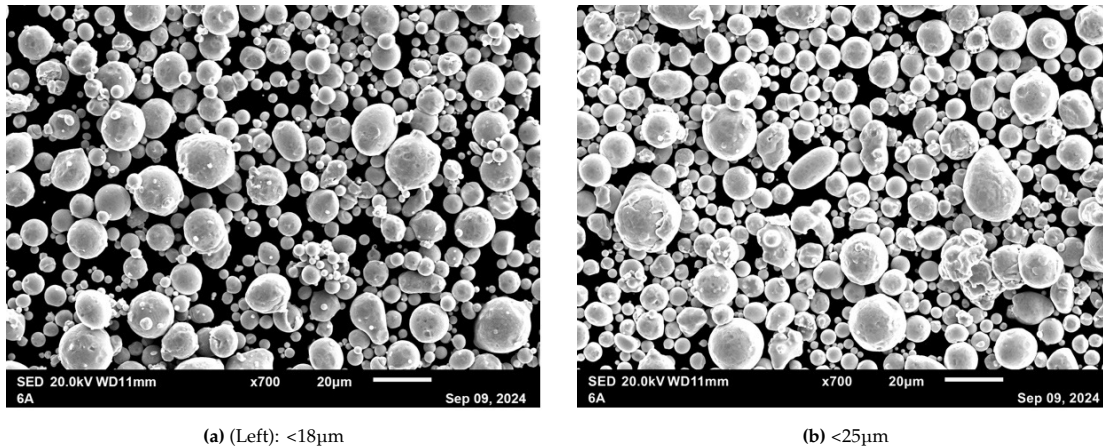


Figure 3.1: Microstructural morphology of 316L S.S Powder by SEM

3.2. Printing and Curing

Prior to printing, the binder jet printer must undergo thorough cleaning and calibration. First, it is crucial to ensure that no other powders or larger contaminants (e.g., fibers and small screws, etc.) are present, as they could disrupt the powder bed structure, and the printing head must be free from blockages caused by high-viscosity organic binders or powders. Second, it is essential to verify that the binder system can function well to avoid issues like uneven binder distribution that could disrupt the printing process. Finally, the flow characteristics of the binder should be checked to avoid potential blockages in the binder delivery system, which can occur due to factors such as low temperatures leading to reduced binder flow.

Printing is the key step in sample preparation with parameters including layer thickness, saturation level, powder spreading, print speed, and print orientation, etc. The printer is provided by Concr3de.

Layer thickness refers to the height of the powder bed along the Z-axis during the printing process, and it typically ranges from 15 to 300 μm for binder jet printing[27]. The smaller the layer height is, the higher accuracy the printing can have, but a longer time the printing will take. The number of layer height will be fixed as 100 μm for this project.

Binder saturation level can be expressed as $S = V_{binder} / V_{air}$, where V_{binder} is the volume of binder, and V_{air} is the volume of open spaces such as pores in the powder bed[54]. Within this project, the saturation level is determined by the waveform of the binder and the X-speed of the printhead. Concr3de designs specific waveforms for different binders. Using a dropwatcher, the behavior of binder droplets and their precise volume ($V_{droplet}$) in picoliters at various X-speeds can be monitored and analyzed. This volume can then be converted into a percentage of saturation level. Based on the previous research from Concr3de, the conversion formula is provided (Equation 3.1 to 3.4), where R represents the resolution of the printhead (400 drops/inch) and PR denotes the packing density of the powder bed (can be

measured).

$$\text{Saturation Level} = \frac{V_{\text{droplet}}}{V_{\text{air}}} \quad (3.1)$$

$$V_{\text{air}} = (1 - PR) \times V_{\text{voxel}} \quad (3.2)$$

$$V_{\text{voxel}} = \frac{\text{Layer Height}}{R^2} \quad (3.3)$$

$$PR = \frac{\text{Powder Bed Density}}{\text{Powder Material Solid Density}} \quad (3.4)$$

The relevant parameters that can be directly obtained are listed in Table 3.5. It should be noted that, due to the printer's inconsistent performance, this experiment adopted relatively stable printing parameters. Consequently, different combinations of printing parameters are not intentionally tested. Specifically, when testing the saturation level, the corresponding layer height is 100 μm , the waveform is 3-pulse mode (3P) for the Metal binder, the X-speed is 20%, and the spread Z-axis offset is 1 mm. The X-speed stands for the moving velocity of printhead in X direction, and it is given in percentage with the maximum value of 500mm/s. Besides, the maximum roller speed is 120 rpm.

Table 3.2: Parameters and relevant values for saturation level test

Printing Parameters	Picked Values
Layer Height	100 μm
Waveform	3 Pulses
X-Speed	20%
Z-axis Offset	1mm
Printer head resolution (R)	400 DPI

To measure the packing bed density, cups with 1x1x1 cm^3 space and 0.5 cm wall thickness within the powder bed are printed. The mass of the powder inside the cup is then measured and divided by the volume (1 cm^3) to obtain the packing bed density. The advantage of this approach is that the powder filling density within the cup closely replicates the packing density during the printing process. However, due to the small size of the cup, there could be shear effects between the cup walls and the powder, which could influence the natural packing of the powder within the cup. The results of the packing density can be seen in Table 3.3.

Table 3.3: Data of packing bed density

	1	2	3	4	5	Average
Mass/g	5.37	5.46	5.51	5.60	5.55	5.50
Volume/ cm^3	1.00	1.00	1.00	1.00	1.00	1.00
Density/ g/cm^3	5.37	5.46	5.51	5.60	5.55	5.50

Table 3.4 shows the different values for the droplet size when the x-speed varies for two different waveforms, and Table 3.5 gives the calculated saturation level values (in percentage) for 3P (Only 3P mode is applied in this research). To simplify the calculation, the average value of the droplet size for 30% X-speed is taken. The value of 3P 60% is extrapolated as the dropwatcher could not give the corresponding droplet size.

Table 3.4: Parameters of different waveforms for Metal Binder

X-speed	2 Pulse (2P)/pL	3 Pulse (3P)/pL
10%	78–85	85–105
20%	85–105	115–125
30%	115–125	130–140
40%	120–130	140
50%	125–145	Unstable
60%	130–140	Unstable

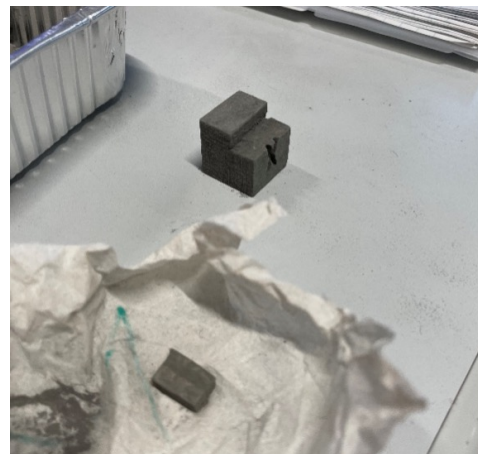
Table 3.5: Saturation level under 3P mode

X-Speed (%)	Saturation Level (%)
20	96
30	108
60	140

3.3. Debinding and Sintering

Debinding and sintering connect printing step with post processing step. The binder within green samples should be removed sufficiently, and sintering stimulates the bonding of particles to form a good densification. To analyze both thermal debinding behavior of metal binder and sintering effect of printed 316L stainless steel samples within argon atmosphere, the thermogravimetric analysis (TGA) is employed. The reduction of mass indicates the decomposition of binder, and with thermogravimetric analysis (TG) and derivative thermogravimetry (DTG) curves the start and finish debinding temperature can be obtained.

The TGA equipment applied is the Themys Duo made by Setaram [90], as shown in Figure 3.2a. It should be noted that the temperature measured by the thermocouple is typically inaccurate, with the actual temperature inside the TGA chamber being higher than the recorded value, since the thermocouple inside the TGA instrument needs to be wrapped in protective material when exposed to hydrogen or argon environments at temperatures exceeding 1000°C within the chamber. Additionally, due to the large size of the green sample, a small section is cut from the green part with a saw for analysis in the TGA, as shown in Figure 3.2b.

**(a)** TGA Machine applied**(b)** Sample part for TGA analysis**Figure 3.2:** TGA Testing equipment and sample piece

After obtaining the temperature corresponding to the sample's mass change through TGA, the sample can be placed in a furnace for debinding and sintering, which can be performed sequentially in the

same furnace. The furnace used in this project is the LHTG 200-300/22-1G, manufactured by Carbolite Gero, with a temperature range of 30-3000°C, as shown in Figure 3.3. The flow rate of protective gases (e.g., nitrogen, argon) can be set between 50-500 L/h. The internal volume of the furnace is 10 liters, and the samples are placed on a graphite tray [91]. The whole debinding and sintering profile is shown in Figure 3.4, and the flow of Ar is 150 L/h.

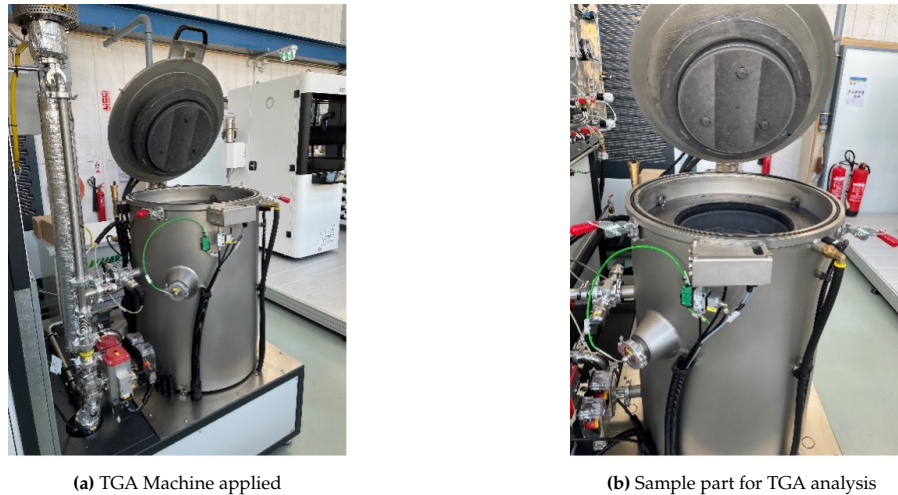


Figure 3.3: Furnace for debinding and sintering

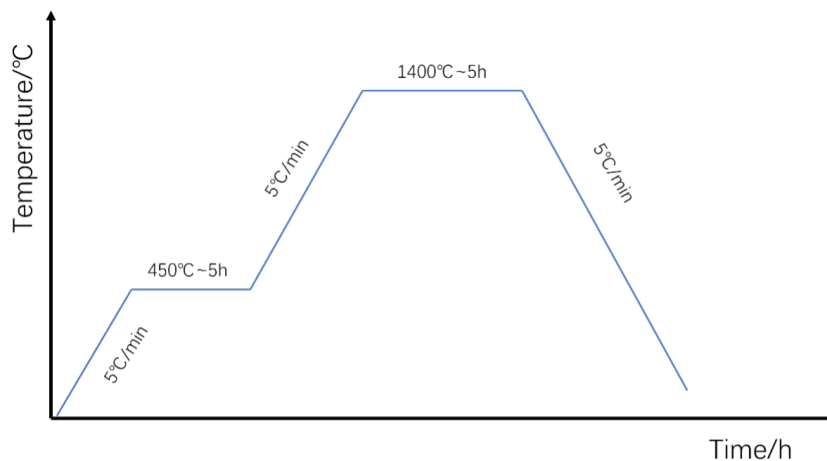


Figure 3.4: Profile of Debinding and Sintering

3.4. Characterization

3.4.1. Dimension Test Equipment

Both a laser scanner and caliper used to measure sample dimensions for comparison purposes. The laser scanner utilized is the Artec Space Spider, as shown in Figure 3.5a. This scanner's advantage lies in its ability to generate 3D models, which can be converted into STL files for use with 3D printers. However, the scanning results are less than ideal. During the scanning process, the sample needs to be placed on a platform that can rotate 360 degrees, while the scanner is held stationary by the operator. After sequentially scanning all surfaces of the sample, the software merges the scans to create a final 3D model. If the sample's surface is too dark, reflective, or smooth, a texture spray can be applied to

reduce reflections or distinguish different surfaces to aid in measurement. However, the spray may form a white coating on the material's surface, which could negatively affect surfaces with fine details. The technical specifications of the Spider scanner [92] are provided in Table 3.6

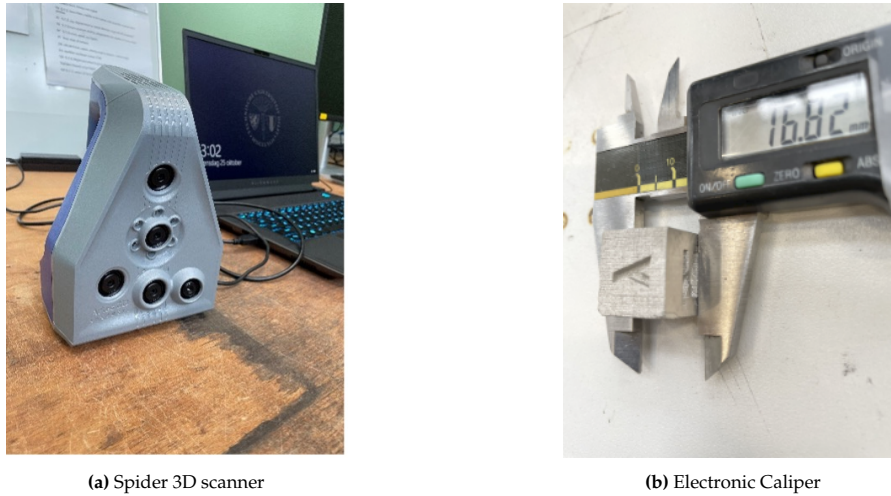


Figure 3.5: Dimension Test Equipment

Table 3.6: Specifications of Artec Space Spider 3D Scanner

3D Accuracy	0.05 mm
3D Resolution	0.1 mm
Data Processing Algorithms	From 5 mm
Output Formats: 3D Mesh	OBJ, PLY, WRL, STL, AOP, ASC, PTX, E57, XYZ, RGB
Output Formats: CAD	STEP, IGES, X_T
Output Formats: Measurements	CSV, DXF, XML

Although the green part cubes had edge lengths of approximately 2 cm, which should be proper enough to minimize scanning errors, the Spider scanner is unable to accurately capture the volume of the green samples due to engraved letters on the surface, which are used to mark the printing orientation. As a result, the 3D models generated by the Spider scanner are not suitable for subsequent density measurements. Given that using the Spider scanner is more time-consuming compared to using calipers, this study opted for calipers when measuring sample dimensions (Figure 3.5). The calipers have a resolution of 0.01 mm and allow for relatively efficient measurement of the cube samples. For the measurement, three-point method is used, as shown in Figure 3.6. In the coordinate system, XD and YD represent the X-direction and Y-direction during printing, respectively, and ND refers to the direction perpendicular to the XY-plane.

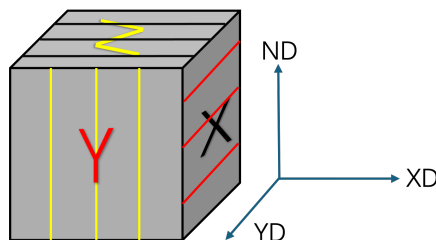


Figure 3.6: Calculation of Saturation Level

3.4.2. Density Test Equipment

In this study, two methods can be used for density measurement of cubic samples, the Archimedes method and the mass-volume method using calipers and a scale. Due to the potentially high porosity of the binder jet-printed samples, and in accordance with the ISO 2738 standard "Sintered metal materials, excluding hard metals — Permeable sintered metal materials — Determination of density, oil content and open porosity," samples need to be impregnated with oil [93]. Therefore, obtaining the volume by immersing the samples in water may theoretically result in errors due to an overestimation of the volume. The mass-volume method, which involves measuring the dimensions with calipers and calculating the density by dividing the mass by the volume, may yield more accurate results compared to the Archimedes method. However, due to the presence of engraved letters on the sample surfaces, the calipers cannot accurately measure the volume occupied by the engravings. As a result, the Archimedes method is ultimately selected for density measurement in this experiment. To investigate whether directly submerging the green parts in water would yield different density measurements, WD-40 was applied to the surface of two green parts to prevent water from penetrating the samples. However, the final measurements showed no significant difference compared to the green parts that were not treated with WD-40.

Given the experimental constraints, water is used as the immersion fluid, and efforts are made to ensure the samples are fully submerged in water until no air bubbles are visible on the surface. To verify the internal density distribution of the samples, three sintered samples are cut into four sections each (Figure 3.7a), and the density of each section is measured separately, with the result being the average of all measurements. The Archimedes method measurement apparatus designed for this experiment is shown in Figure 3.7b, and the equipment is Mettler pm 480 delta range.

Finally, Rhino 8 is used to determine the volume of cube models in stl. file. The theoretical green part density then can be calculated by dividing the measured mass of the green part by this volume.



(a) Sample for density distribution test



(b) Archimede's method for density measurement

Figure 3.7: Density Test

3.4.3. XRD

To investigate the oxidation of sintered samples, X-Ray Diffraction (XRD) is applied to check the diffraction peaks of relevant phases, namely those of iron oxide. The specific instrument is Bruker D8 Advance diffractometer Bragg-Brentano geometry with graphite monochromator and Vantec position sensitive detector. Co $K\alpha$ radiation is used, with divergence slit V12, scatter screen 10mm, 40kV 40mA. There is no sample spinning. The measurement is coupled θ - 2θ scan with a step size of $0.035^\circ 2\theta$, and the counting time per step of 2s. The software for data analysis is the Bruker software DiffraSuite.EVA

vs 7.1.

3.4.4. SEM and OM

The microstructure information including porosity, metallographic structure of sinter samples is investigated with Scanning Electron Microscope (SEM, JSM-IT100) and VHX 7000N Digital Microscope. And Energy-Dispersive X-ray spectroscopy (EDS) function of SEM is also used for element analysis.

Before characterization through microscopy, 316L stainless steel samples require to be prepared through the following steps: embedding, sanding, polishing, and etching. Cutting may be required if samples are oversized. Since SEM is involved, samples are embedded with conductive polymer materials. Then, sanding with sandpaper of the proper grit size, namely 180, 320, 1200, and 2000 (2 minutes for each size), and polishing (3 μm for 2 minutes and 1 μm for 3 minutes) are needed. For the etching step, the chemical solution is Sigma-Aldrich 37% HCl: Sigma-Aldrich 65% HNO₃: H₂O (deionized) in a ratio of 1:1:1 for 30 seconds. The calculation of grain size was performed using the software ImageJ, employing the traditional Line Intercept Method.

3.4.5. Mechanical Properties Test

Mechanical tests show the mechanical properties of samples. For this project, hardness test and compression test are done. Vicker hardness tester and materials testing machine (Zwick Z100) are used. To satisfy the requirement of equipment, polished samples were applied for hardness test, and small samples (side length is less than 1cm) were used for compression test. The Z100 universal testing machine supports a maximum load capacity of 100 kN and is suitable for a wide range of sample sizes. However, limitations include stress concentration issues in samples with inscriptions or letters, and challenges in testing oversized samples exceeding 1.5 cm in size. For the Vickers hardness tester, it is ideal for small-area samples due to its small and symmetrical indentations, providing relatively precise results. Its high level of standardization ensures comparability with results from other hardness testing methods.

4

Results and Discussion

To ensure consistency with the overall experimental workflow, the subsequent sections will be organized as follows: printing and curing, TGA, debinding and sintering, characterization (including XRD, dimensional measurements, density, and microstructure), followed by mechanical tests, which will include hardness test and compression test.

4.1. Optimization of Green Body Printing Parameters

The printing phase consisted of three sessions. The goal of the first session was to evaluate the performance of the machine with 316L stainless steel powder and metal binder in order to optimize the printing parameters. The second and third sessions required recalibration of the printing parameters due to machine replacements, while also refining the printing and curing parameters based on the findings from the first session.

4.1.1. Printing of Green Body

The printing parameters utilized in this study are detailed in Appendix 1. A total of four batches were printed, with each batch containing nine samples. During the depowdering step, samples from the first and second batches frequently exhibited morphological defects (e.g., deformation of lettering), surface delamination (Figure 4.1a), and insufficient bonding strength (Figure 4.1b) due to the instability of the binder system. As a result, only approximately 3-4 samples per batch had relatively intact surfaces, with most defective samples located near the edges of the printing platform (Figure 4.2), whereas those positioned at the center were comparatively intact. Following adjustments to key parameters, including powder spreading speed, X-axis speed of the printing head, and feed height, the overall quality of the third batch showed significant improvement. However, minor defects remained in specific areas, such as lettering deformation and uneven surfaces. Nevertheless, the edge integrity and dimensional accuracy of the samples were notably enhanced compared to those in the first two batches.

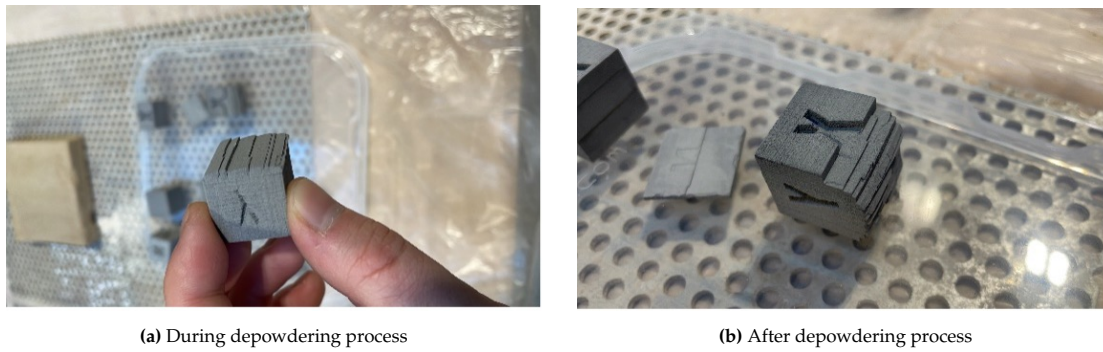


Figure 4.1: Delamination of green parts before and after depowdering process

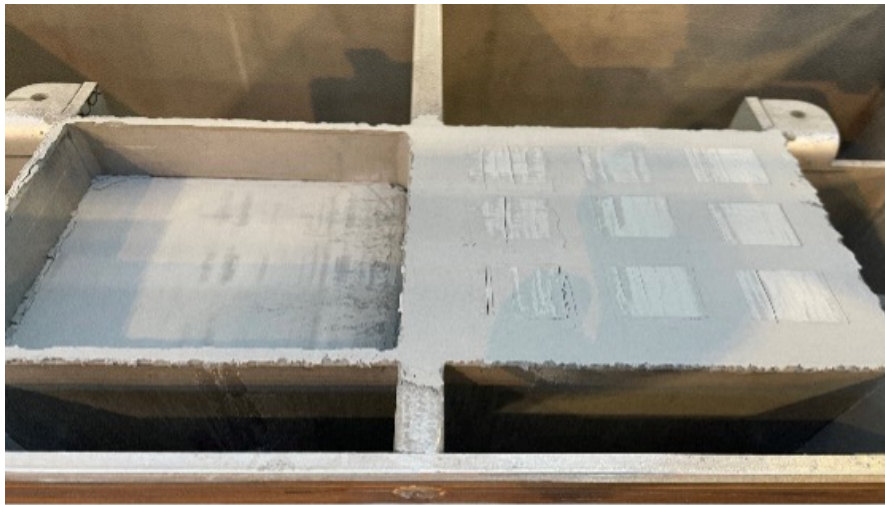


Figure 4.2: Edge samples exhibited more defects compared to central samples

As shown in Figure 4.2, significant cracking was observed on the powder bed surface of the printing platform during the printing process, with the most severe cracks occurring in the leftmost printing region. Although the rightmost printing region appeared visually to exhibit fewer cracks, the samples produced in this area still displayed notable surface delamination and, in some cases, cracking. The most structurally intact samples were located in the central region, where no cracking or damage was observed after the depowdering process. However, these samples still exhibited relatively high surface roughness and lower dimensional accuracy.

Figure 4.3 illustrates the powder leakage along the edges of the platform during the printing process. This issue arises because the square silicone sealing gasket used for sealing is slightly smaller than the frame of the platform. This design choice was made to slightly compromise the dimensional accuracy of the gasket to reduce friction between the platform and the surrounding frame during the printing process, as excessive friction could cause the platform to stop moving vertically. However, the resulting powder leakage likely led to stress concentrations along the edges of the powder bed as the platform descended, thereby resulting in the initiation and propagation of cracks. This ultimately resulted in the

surface defects observed in Figure 4.2, increasing the likelihood of sample fracture.



Figure 4.3: Powder leakage at the edge of printing platform during printing process

In addition to powder leakage, the spreading roller may introduce varying degrees of defects during the powder spreading process due to two primary reasons. First, small amounts of binder adhered to the roller surface can cause localized powder clusters to form on its otherwise smooth surface. These clusters, as the roller rotates during spreading, may create scratches on the powder bed surface, thereby reducing its overall integrity. Second, the structural instability of the roller's fixed end can result in unintended vertical tapping as the roller retracts to its original position after spreading. This tapping may disturb the evenly spread powder bed by displacing localized areas of powder, leading to uneven powder distribution and, consequently, a reduction in printing accuracy.

Furthermore, suboptimal binder spraying contributed to the low completion rate of the first batch of samples, with the following factors identified. First, clogging occurred within the binder transport pipelines or at the nozzle, resulting in the printhead failing to discharge binder. This issue is likely exacerbated by the high viscosity of the custom-developed binder combined with low ambient temperatures during winter, which reduce the flowability of the binder and hindered its participation in the printing process. Second, the pump responsible for extracting binder in the binder system malfunctioned, leading to insufficient binder discharge. This inadequacy prevented adequate interlayer bonding, ultimately causing sample failure. Figure 4.4 shows one of the binder spraying results. Compared to the ideal continuous binder line in Figure 2.9b(c), the actual binder trajectory exhibited a discontinuous, dotted pattern. Moreover, under the same waveform, the binder trajectories produced by different nozzles on the same printhead varied significantly. This inconsistency substantially increases

the possibility of weak interlayer bonding.

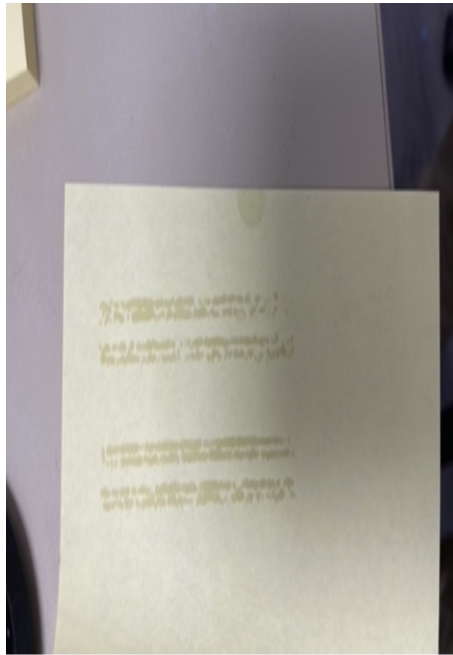


Figure 4.4: Suboptimal binder line

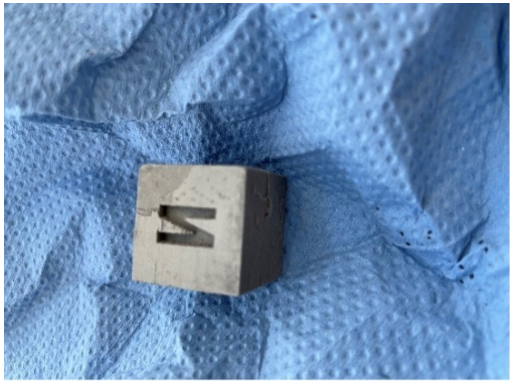
4.1.2. Effect of Printing Equipment

Due to the replacement of the printer, both hardware components (e.g., the powder spreading roller) and software settings (e.g., printing parameters) required recalibration. The printing parameters established for this experiment are detailed in Appendix 1. The integrity of the samples produced in this session was superior to those from the first experiment. To evaluate the impact of different binder waveforms on printing quality, both 2P and 3P modes were tested. While samples printed using the 2P waveform exhibited good dimensional accuracy and surface detail prior to curing, they were highly prone to disintegration into powder after curing. Consequently, all subsequent prints employed the 3P mode.

Although the 3P mode improved printing accuracy (Figure 4.5a) and sample durability, sample integrity remained inconsistent across the three print runs, with common defects such as high surface roughness and even surface (see Figure 4.5b). Additionally, an attempt was made to print 12 dog-bone specimens arranged in a stacked configuration consisting of four layers and with three specimens per layer (Figure 4.6a). However, severe cracking was observed on the powder bed surface near the edges of the printing platform (Figure 4.6b), leading to the failure of all dog-bone specimens due to fracture after curing. As the printing platform is confined to a fixed size of 10 cm x 10 cm and cannot be expanded, adjustments such as modifying the distance between the spreading roller and the powder bed, altering the X-axis speed, or changing the orientation of the dog-bone specimens were ineffective in mitigating cracking or preventing subsequent specimen failure.

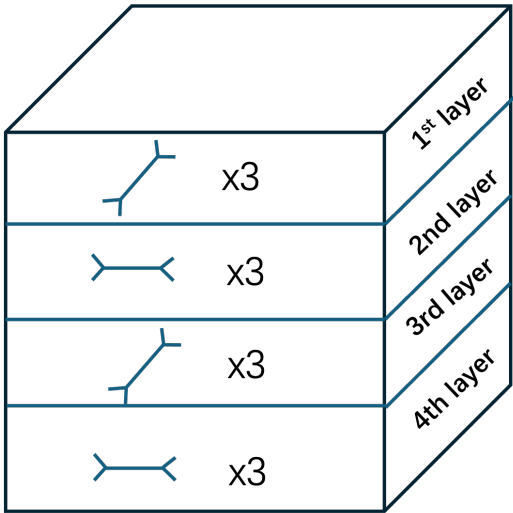


(a) Better powder bed surface than the 1st batch



(b) Surface self-delamination

Figure 4.5: Samples of the 2nd batch



(a) Dog-bone arrangement



(b) Edge cracks make dog-bone fracture

Figure 4.6: The printing of dog-bone components

The observations during the printing process reveals that edge powder leakage and surface cracks on the powder bed were still present (Figure 4.7), and which indicating that the sealing around the printing platform and the roller surface may exhibit similar flaws to those observed in the first batch. Examination of the binder line shows that although the binder trajectory remains suboptimal, the saturation have improved compared to the first batch (Figure 4.8).



Figure 4.7: Powder leakage and cracks during the printing

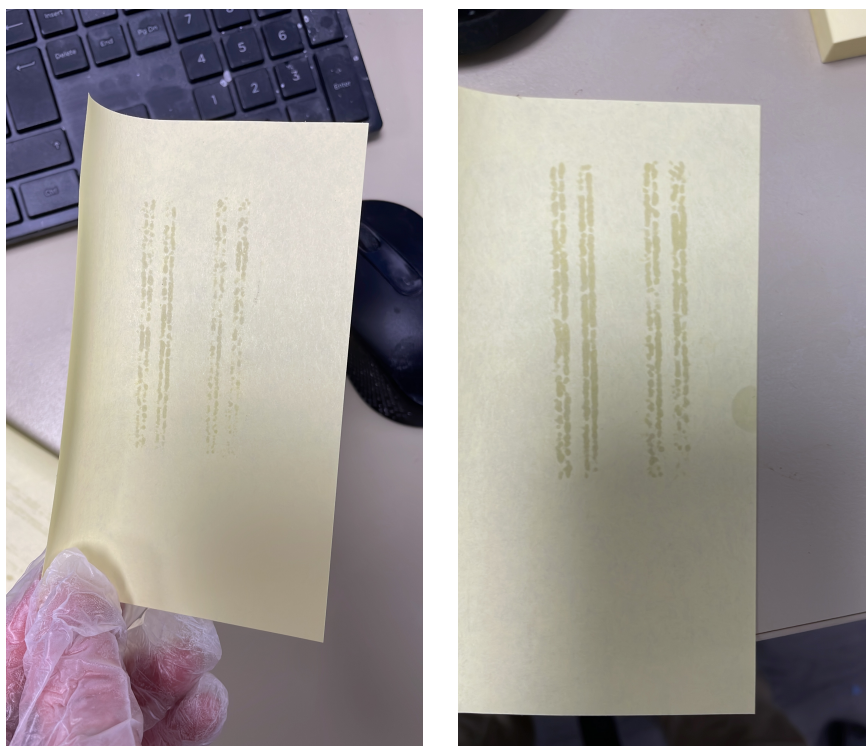


Figure 4.8: Binder lines during the 2nd printing

4.1.3. Calibration of Printing Parameters

The printer for the third session is the calibrated version of the printer from the first session, and the printing parameters followed those detailed can also be found in Appendix 1. Two batches of samples were printed in this session: cups for testing packing bed density (with an internal volume of 1 cm^3) and plain cubes with an edge length of 1 cm. Although visible cracking and roller-induced surface defects were observed during the test prints of 5 cm cubes (Figure 19), no significant cracking was observed during the actual printing of those mentioned samples. Additionally, the powder bed surface

on the printing platform appeared relatively smooth (Figure 20a). The cup models used for packing bed density testing and final cube samples are shown in Figure 4.10a and 4.10b.

The defects in green parts include surface defects and improper bonding, which reflects potential issues in the printing process. During the printing process, parameters such as layer thickness and feed height are kept consistent unless necessary adjustments are required. Therefore, the issues that arise during printing primarily stem from the binder system and the powder bed.

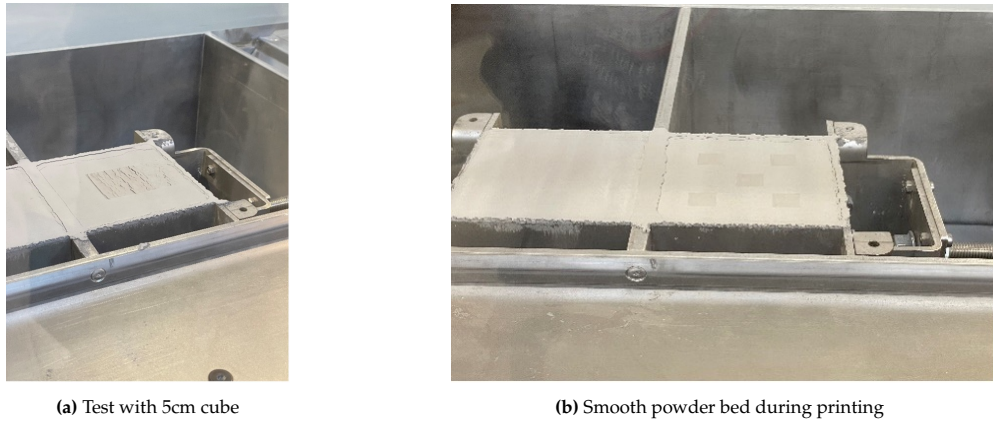


Figure 4.9: The 3rd printing session

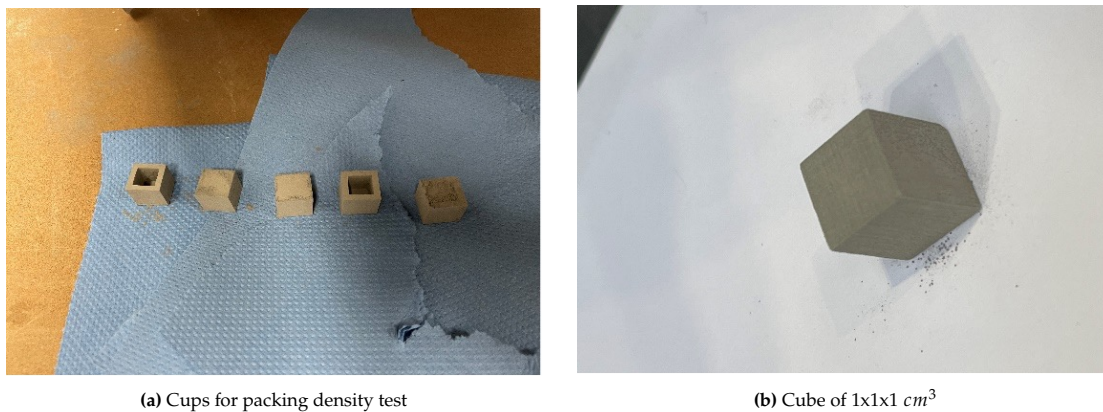


Figure 4.10: Small cups for packing density test and the final small cubic samples

Based on the three printing processes conducted, several critical parameters will be analyzed, starting with the binder. Although the composition and manufacturing process of the binder are proprietary, maintenance technicians have recommended heating the binder to ensure smooth transport through the pipelines. This indicates that the binder possesses high stability, viscosity, and low volatility. However, these properties also increase the likelihood of nozzle clogging, which can hinder proper binder deposition, compromise the integrity and precision of the printed pattern, and potentially result in defects such as cracks, ultimately reducing the mechanical performance of the printed parts [94]. Additionally, to minimize airflow interference during the descent of binder droplets, the distance between the printhead and the powder bed is typically set to 1–3 mm. However, in this study, the printer's printhead-to-powder bed distance is approximately 5 mm, which may expose binder droplets to airflow disturbances. Such disturbances could negatively impact the interaction between the binder droplets and the powder bed [71].

Then it is the powder bed. When using a counter-rotating powder spreading roller, the roller exerts a compacting effect on the powder bed, and as the layer thickness decreases, this compacting effect intensifies, which can help increase the green part density. However, when the layer thickness is too

low, the spreading process may introduce defects, such as overall part shifting and the formation of large voids within the green part, both of which can reduce the part's density[95]. Additionally, the shear forces generated by the powder roller can cause layer misalignment in the printed part, leading to deformation or even failure. If the compacting effect of the powder roller is limited (as shown in Figure 4.9a and 4.2), combined with uneven binder deposition or a low saturation level, the packing density of the powder bed and interlayer bonding quality may be compromised, increasing the likelihood of defects in the green part.

In this experiment, due to machine changes, the layer thickness was kept at 0.1 mm and the feed height at 0.20 mm (except for the third batch, where it was adjusted to 0.18 mm). The X-speed ranged from 10% to 30%, and the roller speed was set between 25% and 50%. As for the selection of layer thickness, the minimum layer thickness in BJ is typically three times the average particle size and should exceed the largest particle[87]. The two powders used in this experiment had particle sizes of $>18\ \mu\text{m}$ and $>25\ \mu\text{m}$, respectively, making the $100\ \mu\text{m}$ layer thickness appropriate. Previous studies indicate that layer thickness and binder saturation have the greatest impact on green part quality[42], so the effects of X-speed and roller speed will not be discussed here.

4.2. Densification of Green Body

4.2.1. Effect of Sintering Temperature

To determine the debinding and sintering temperatures for the 316L stainless steel samples, thermogravimetric analysis (TGA) is employed in this experiment. As shown in Figure 3.2b, a small portion of the sample was extracted from the larger cubic sample to meet the capacity requirements of the alumina crucible inside the TGA. The selected samples and their corresponding temperatures are listed in Table 4.1. And, the melting point of this selected SS 316L powder is between $1420\ ^\circ\text{C}$ to $1440\ ^\circ\text{C}$.

Table 4.1: TGA testing data

Sample	Debinding		Sintering		Atmosphere	State	Relative Density/%
	Temp/ $^\circ\text{C}$	Time/h	Temp/ $^\circ\text{C}$	Time/h			
1	400	3	1380	5	Ar	solid	97.16
2	400	3	1400	5	Ar	solid	97.82
3	400	3	1400	10	Ar	solid	96.74
4	400	3	1420	5	Ar	solid	94.51
5	400	3	1440	5	Ar	molten	98.03

An analysis of the TGA results was conducted using Sample 4 as a representative example. The entire process, including debinding, sintering, and temperature-changing steps, lasted approximately 18 hours. Figure 4.11 shows the relationship between mass change and temperature for a small sample placed in the TGA. The green line represents the mass, corresponding to the right y-axis (in milligrams), while the orange line represents the temperature, corresponding to the left y-axis (in $^\circ\text{C}$). Figure 4.12 includes a purple line, which represents the derivative of the green line (mass). A noticeable drop in the derivative indicates significant mass loss.

By examining both figures, it can be observed that the two regions marked with red circles show significant mass loss. The first major drop in mass (green line) occurs within the first hour, corresponding to a temperature of approximately $400\ ^\circ\text{C}$. The second significant mass loss happens between the 6th and 9th hours, with the fastest rate of loss occurring at around $1300\ ^\circ\text{C}$. However, the mass stabilizes around the 9th hour, at which point the temperature reaches $1400\ ^\circ\text{C}$. As shown in Table 4.1, the melting of the 316L stainless steel sample occurs at $1440\ ^\circ\text{C}$.

Therefore, after more than five experiments, to ensure the complete removal of the binder, $450\ ^\circ\text{C}$ and

1400°C were selected as the debinding and sintering temperatures, respectively.

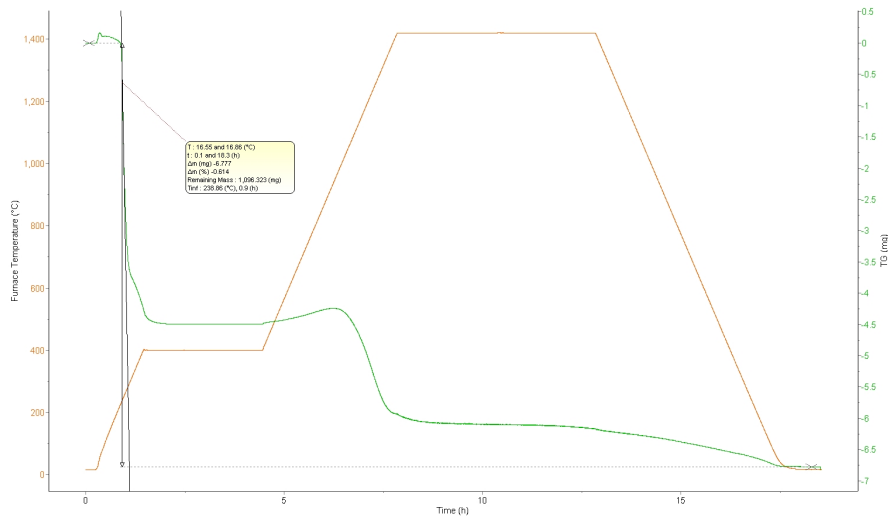


Figure 4.11: TGA data of sample 4

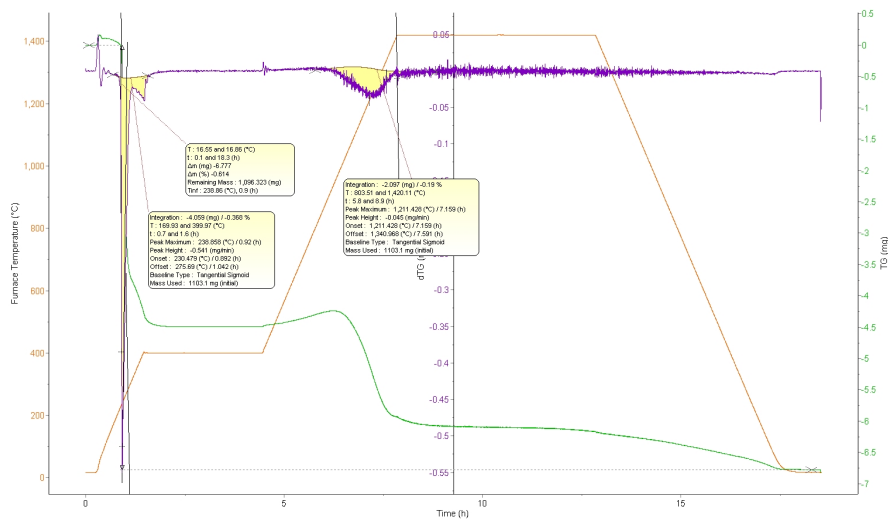


Figure 4.12: TGA data and derivative of sample 4 mass variation

4.2.2. Effect of Debinding and Sintering Atmosphere

Based on the TGA data, the debinding and sintering profile is developed, as shown in Figure 3.4. Sintered samples can be seen in Appendix 2. During sintering, two atmospheres were employed: Argon (Ar) and vacuum. For the first session samples (smaller than 18 micrometers), nine samples with the best surface morphology and dimensions were selected, five of which underwent TGA analysis. Therefore, the remaining four samples were sintered according to the post processing profile. The sintered samples are shown in Figure 4.13a.

In the second session, although different powder with a particle size of less than 25 micrometers and a different printer were used, the same sintering strategy was applied due to time constraints and sample quantity considerations. In this case, two samples were selected for sintering, one in an Ar atmosphere and the other in a vacuum. The results showed differences in hardness and microstructure. However,

further research is needed to determine whether these differences were solely due to the sintering atmosphere.

In the third session, nine samples were produced, five of which were sintered in an Ar atmosphere, while the remaining four were sintered in a vacuum. However, due to an issue with the furnace's gas supply during the sintering process, the surfaces of the four samples in the vacuum atmosphere oxidized and turned black, as shown in Figure 4.13b.

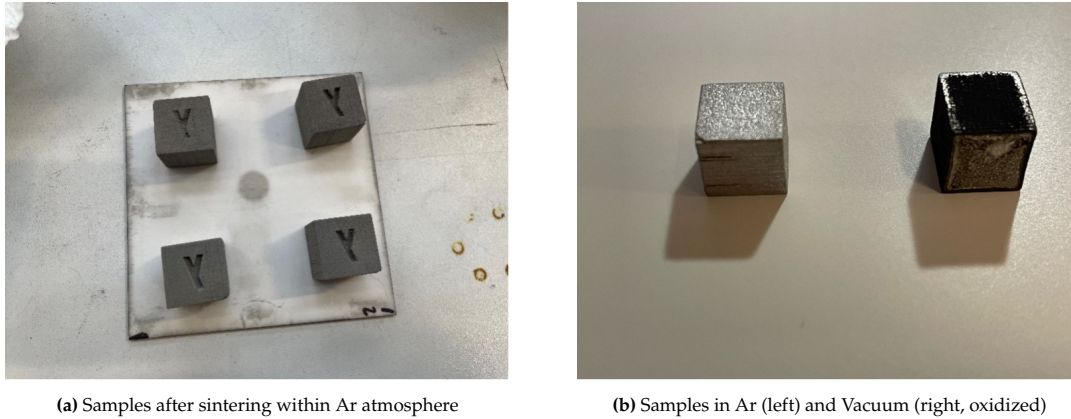


Figure 4.13: Samples sintered within different atmosphere

Sintering is a key process to enhance the density and strength of BJ metal parts, allowing control over porosity and mechanical properties. The process is divided into four stages: the green part stage, initial sintering, intermediate sintering and final sintering. In this experiment, sintered samples achieved a relative density above 94% using the Archimedes method. Despite expectations for decreased porosity due to grain boundary migration at around 1410°C, SEM and OM images still show dispersed pores. However, compared to the samples sintered in argon flow, the samples sintered in vacuum exhibit significantly lower porosity. Thus, those pores may be caused by the argon trapped in closed pores during sintering and they expand at high temperatures[85]. Further discussion on the porosity generated during sintering will be provided in Section 4.7.

4.3. Microstructural Characterization

4.3.1. XRD

XRD is employed to analyze the chemical composition of the samples to determine whether oxidation had occurred or if any organic residues remained. The XRD results are presented in Figure 4.14. Two samples exhibit similar characteristics, with both showing FCC austenite as the primary phase (labeled as '304 stainless steel' in the legend, representing the FCC structure) and BCC as a secondary phase. A small peak is observed around $2\theta = 46^\circ$, which is identified as a k-beta peak from the main FCC phase, rather than from a different phase. This phase is determined to be γ -austenite associated with the (111) plane [89, 96, 97].

Additionally, very small peaks appear around $2\theta = 55^\circ$, but the corresponding phase could not be identified. For the peaks around $2\theta = 52^\circ$ and $2\theta = 89^\circ$, they are attributed to γ -austenite associated with the (200) and (311) planes, respectively. Several potential phases were explicitly examined, including Cr_2O_3 , Cr_{23}C_6 , Cementite (Fe_3C), Fe_2O_3 , and Cr_3O_8 , but none matched the measured patterns, as some characteristic peaks were missing. However, at $2\theta = 60^\circ$, an additional peak is observed compared to the studies by Yan and Xu et al. Given that the powder has been recycled at least twice, this peak is likely attributed to surface contamination [89, 96, 98]. In summary, oxidation or residual binder cannot be directly identified from the XRD results.

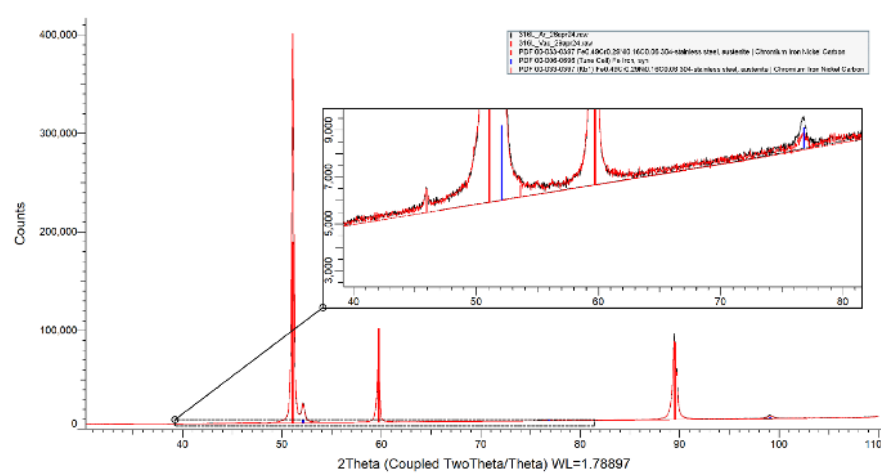


Figure 4.14: XRD result of 316L stainless steel samples sintered within Ar and vacuum

4.3.2. Microstructure

For powders applied in binder jetting, spherical powder particles offer high packing density and good flowability, and powder's particle size distribution (PSD) affects the porosity, pore size, and its distribution. As shown in Figure 3.1, both powders exhibit a high degree of sphericity. Figure 4.15 presents the SEM view of the powder arrangement in the unsintered green part ($<18\ \mu\text{m}$), revealing that many fine powder particles are unevenly distributed around larger particles. While the presence of fine particles reduces pore size and enhances particle bonding, their uneven distribution can lead to non-uniform pore structures. Additionally, the small size of bonding necks between particles suggests a low binder distribution uniformity, which may result in surface roughness and defects such as delamination or fractures. To improve surface smoothness and enhance interparticle bonding, finer powders, thinner layers, smaller binder droplets, and a more uniform powder bed should be used. Moreover, using a mixture of powders with various particle sizes is an effective approach [69].

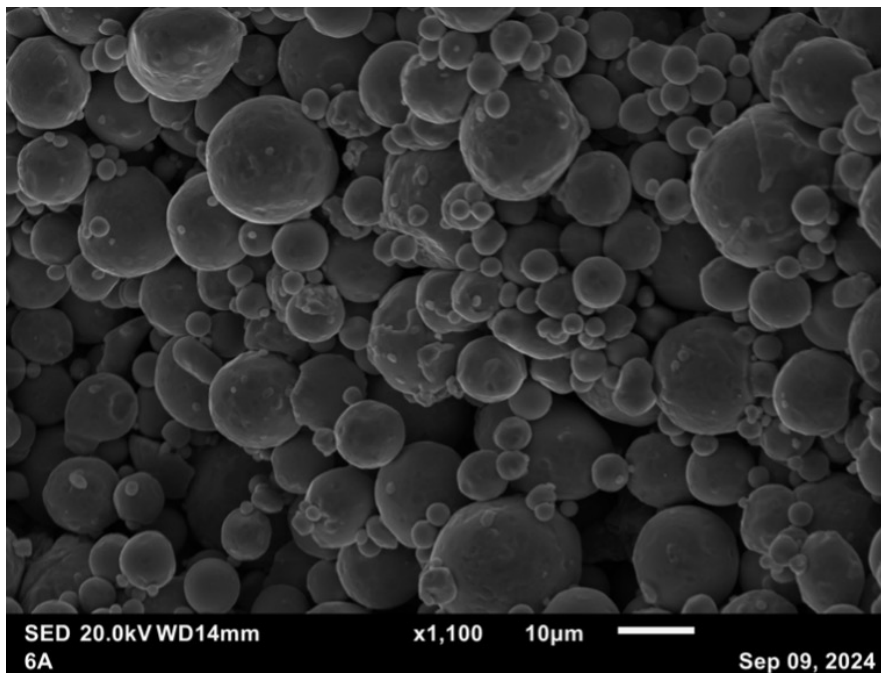


Figure 4.15: Microstructural morphology of green part ($<18\ \mu\text{m}$)

Figure B.2 correspond to three samples with different particle size and sintering atmosphere. Figure 4.16a and Figure 4.16b represent the metallographic microstructures of samples with particle sizes of $18\ \mu\text{m}$ and $25\ \mu\text{m}$, respectively, sintered in an argon atmosphere. In contrast, Figure 4.16c shows the metallographic microstructure of a $25\ \mu\text{m}$ sample sintered in a vacuum atmosphere. These three samples follow the debinding and sintering profile shown in Figure 3.4. All three images display a distinct austenitic structure. However, unlike Figure 4.16c, numerous black spots of varying sizes can be observed in Figure 4.16a and Figure 4.16b and they irregularly distributed throughout the microstructure.



(a) Particle size $<18\ \mu\text{m}$, sintered in Ar



(b) Particle size $<25\ \mu\text{m}$, sintered in Ar



(c) Particle size $<25\ \mu\text{m}$, sintered in Vacuum

Figure 4.16: OM images of 3 samples under different sintering conditions

As seen in Figure 4.17 and the corresponding EDS elemental analysis data in Table 4.3, position 5 is located within the austenitic matrix, position 2 is situated in a larger, irregularly shaped black region, and position 3 and 4 are found in droplet-like structures. Elemental analysis reveals that all four points have a high concentration of iron oxides and very low carbon content. Therefore, position 2 is not a carbide or other precipitate, and position 3 and 4 are not voids. Consequently, it can be concluded that,

except for position 5, the remaining three points are oxides.

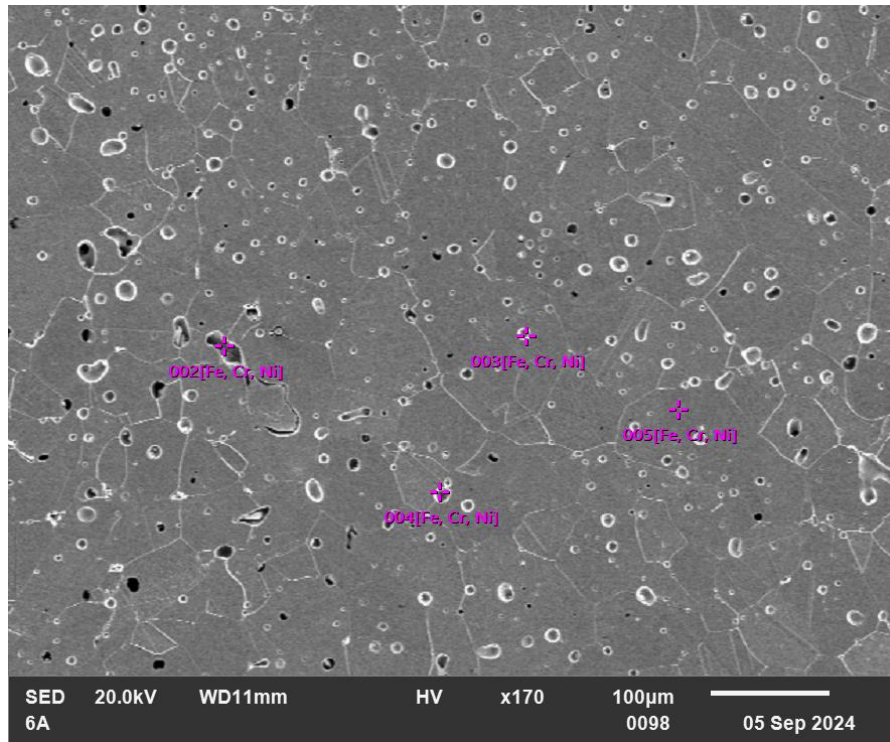


Figure 4.17: SEM analysis about different points of sample <math><18\ \mu\text{m}</math>, sintered in Ar

Table 4.2: Element analysis/Oxide at different points

Position 2		Position 3		Position 4		Position 5	
Formula	mass/%	Formula	mass/%	Formula	mass/%	Formula	mass/%
C	1.60	C	1.62	C	1.61	C	1.59
SiO ₂	0.56	SiO ₂	0.59	SiO ₂	0.69	SiO ₂	0.65
Cr ₂ O ₃	20.12	Cr ₂ O ₃	19.58	Cr ₂ O ₃	20.16	Cr ₂ O ₃	19.73
MnO	1.59	MnO	1.63	MnO	1.67	MnO	11.52
FeO	63.27	FeO	62.82	FeO	62.76	FeO	62.71
NiO	11.01	NiO	11.40	NiO	10.71	NiO	1.52
Ti ₂ O ₃ /MoO ₃	1.85	MoO ₃	2.35	MoO ₃	2.40	MoO ₃	2.30
Total	100.00	Total	99.99	Total	100.00	Total	100.02

To further validate these findings, different areas were selected for EDS elemental analysis, with the results presented in Figure 4.18 and Table 4.3. Area 4 shows a significant accumulation of elements typical of 316L stainless steel, indicating that it is not a void. The elemental composition of Area 3 is nearly identical to that of Area 2, except for the molybdenum (Mo) content. Therefore, Area 3 is unlikely to be a droplet or an external contaminant. Based on this analysis, it can be concluded that these areas

are composed of metal oxides.

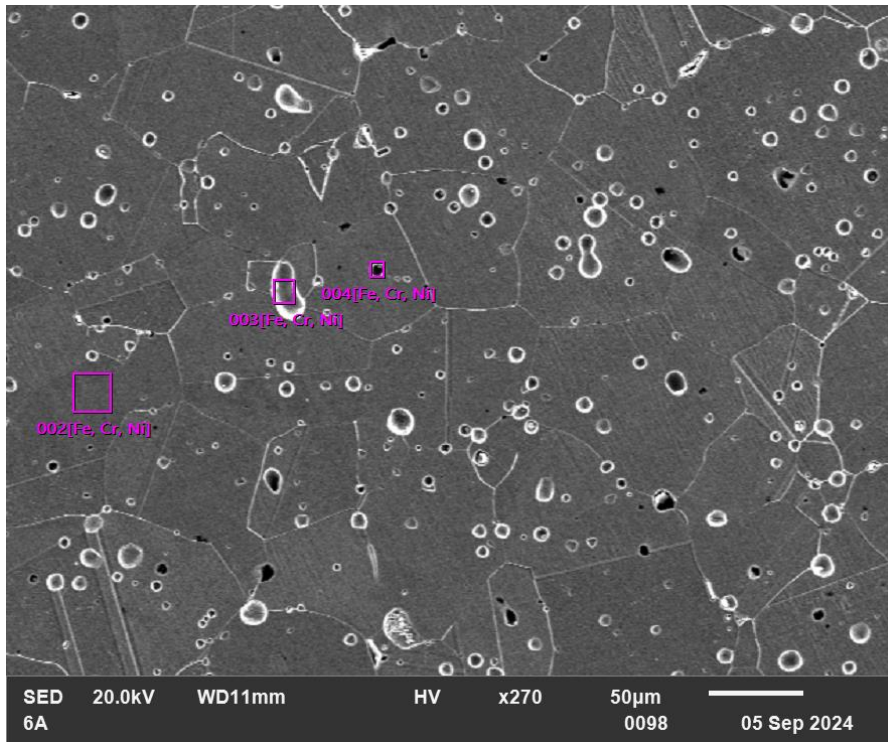


Figure 4.18: SEM analysis within different areas of sample <math><18 \mu\text{m}</math>, sintered in Ar

Table 4.3: Element analysis/Oxide within different areas

Area 2		Area 3		Area 4	
Formula	mass/%	Formula	mass/%	Formula	mass/%
C	0.94	C	0.88	C	0.81
SiO ₂	0.63	SiO ₂	0.67	SiO ₂	0.48
Cr ₂ O ₃	19.85	Cr ₂ O ₃	20.51	Cr ₂ O ₃	20.95
MnO	1.58	MnO	1.88	MnO	2.60
FeO	63.33	FeO	63.69	FeO	63.47
NiO	11.40	NiO	10.41	NiO	9.94
MoO ₃	2.27	MoO ₃	1.97	MoO ₃	1.75
Total	100.00	Total	100.01	Total	100.00

However, aside from the mentioned non-void black spots, SEM analysis of the same sample also reveals the presence of voids. As shown in Figure 4.19, the black area in the center of the image appears to be a void. Using the EDS element mapping function, the distribution of various elements was examined (see Appendix 3). The elemental distribution in the central region appears as a black area, indicating that almost no elements can be detected in this zone. The sample surface has been uniformly treated, and the sample has a relatively uniform density distribution with a value exceeding 95%, it is possible that

the central region is a void.

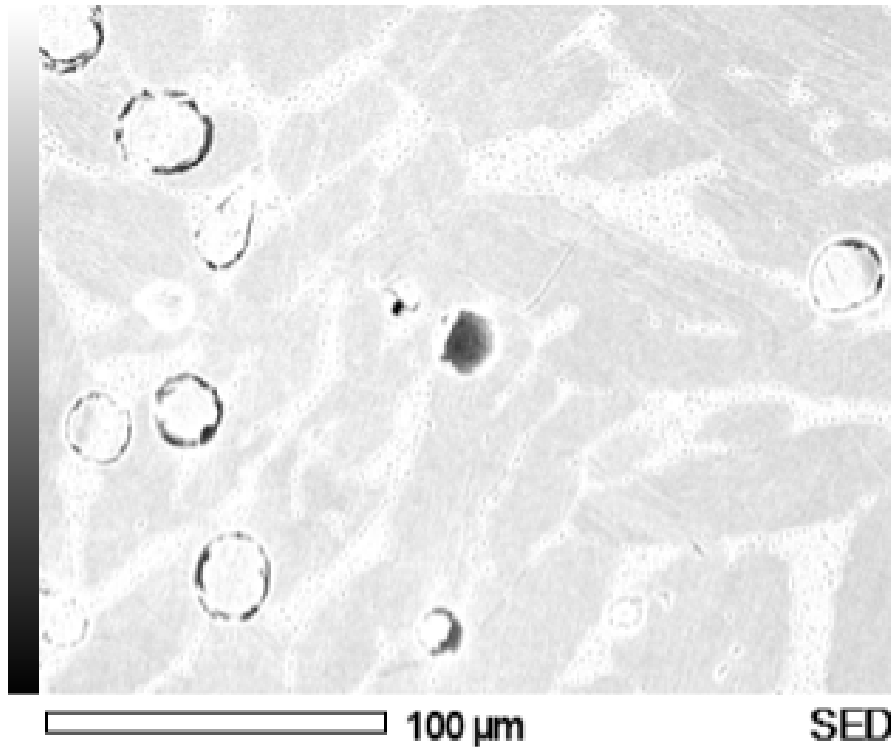


Figure 4.19: SEM image of the selected area

Based on the above analysis, the black spots observed in Figures 4.16a and 4.16b are likely pitting corrosion sites rather than carbon or nitrogen precipitates. For BJP 316L stainless steel, the primary cause of pitting corrosion is the penetration of chloride ions (Cl^-), with increased surface roughness and porosity significantly enhancing the material's susceptibility to such corrosion. Given that the component was manufactured near the Nieuwe Maas River and that an acidic solution containing HCl was used during the immersion stage of sample preparation, there is a potential introduction of chloride ions, though their concentration remains uncertain. The presence of chloride ions likely contributed to the observed pitting corrosion [99]. A potential mitigation strategy to reduce pitting corrosion is to employ superfine finishing techniques to enhance the pitting corrosion resistance of 316L samples.

In this study, insufficient humidity control during sample preparation, combined with high surface roughness and porosity, further facilitated conditions conducive to pitting. Other factors contributing to the observed corrosion require further investigation.

Apart from pitting corrosion, the black spots may also represent different types of pores. As previously discussed, three types of pores can be observed in binder-jetted 316L stainless steel after high-temperature densification (Figure 2.11). Among these, Type III pores are the most prevalent and detrimental. These pores are typically located between layers and aligned perpendicular to the printing direction, acting as potential stress concentration sites. Additionally, Type III pores hinder the densification of binder-jetted metal parts, thereby significantly degrading the mechanical properties of the material. Their formation and prevalence emphasize the need for strategies to address porosity-related challenges in binder jetting processes.

As for the black regions shown in Figure 4.19, based on the EDS elemental mapping results, which indicate a very low presence of elements such as Ni and Fe in these areas, it is likely that these black regions are pores. The relevant EDS mapping can be found in Appendix 3.

4.4. Densification Analysis

4.4.1. Density

Theoretically, the density of a regular cubic sample should be measured using calipers and a scale, followed by a calculation using the corresponding formula. However, due to the presence of engraved lettering on three faces of the sample and the printer's difficulty in accurately producing the sharp edges of the letters, the final density measurement was performed using the Archimedes method.

According to the data of Table 4.4, the density of sintered samples (manufactured with $<18 \mu\text{m}$ powder) is approximately 7.7 g/cm^3 . When compared to the theoretical density of pure iron, which is 8 g/cm^3 , the relative density is around 96%. All four samples here are sintered under the same condition, namely debinding at 450°C for 3 hours, and 1410°C for 5 hours. However, compared to the density values reported in other studies (Table 4.5), the density obtained in this experiment is relatively low, likely due to the high porosity remaining in the samples after sintering. A detailed analysis will be discussed in Section 4.7.

Table 4.4: Density of samples ($2 \times 2 \times 2 \text{ cm}^3$)

Sample	Mass in air (g)	Mass in water (g)	Density (g/cm^3)	Relative Density (%)
Sample 6	37.11	32.27	7.64	95.54
Sample 7	35.54	30.93	7.68	96.02
Sample 8	36.03	31.35	7.68	95.95
Sample 9	35.98	31.31	7.68	96.04

Table 4.5: Density values from 5 studies

Article Author	Density after Sintering (g/cm^3)	Reference
Mao et al. (2023)	7.95	[85]
Mirzababaei et al. (2019)	7.80	[47]
Cabo Rios et al. (2022)	7.95	[88]
Do et al. (2018)	7.90	[31]
Ziaee et al. (2017)	7.85	[42]

Based on the volume calculations from Rhino 8, the volume of a cubic STL file with decorative letters, assuming theoretical dimensions of $2 \times 2 \times 2 \text{ cm}^3$, results in the combined hollow portions of the three letters accounting for approximately 7.705 cm^3 , which is about 3.69% of the total model volume (8 cm^3). Thus, the solid portion occupies approximately 96.31% of the total volume. For data analysis, Table 4.4 and Table 4.6 represent the density data of samples 6 through 9, obtained using the Archimedes method and the mass-to-volume method, respectively. In Table 4.6, the "effective volume" is calculated by multiplying the volume derived from the side length data in Table 10 by 96.31%. A comparison of the two methods reveals that the densities obtained using the Archimedes method are significantly higher than those obtained via the mass-volume method.

Table 4.6: Theoretical values of mass, volume, and density of samples 6–9 with Rhino 8

Sample	Mass in air (g)	Effective Volume (cm^3)	Density (g/cm^3)	Relative Density (%)
Sample 6	37.11	5.10	7.27	90.88
Sample 7	35.54	4.90	7.25	90.63
Sample 8	36.03	4.87	7.40	92.50
Sample 9	35.98	5.00	7.20	90.00

And considering the potential internal porosity of the 3D-printed samples and the possibility of uneven powder packing during printing leading to non-uniform density distribution, three samples are each

sectioned into four parts, and their densities are measured using the Archimedes method. As presented in Table 4.7, although these three samples were printed using different powder particle sizes and sintered in varying atmospheres, their final density distributions exhibit a relatively uniform pattern. Therefore, in subsequent analyses, the assumption that all samples used in this experiment have relatively uniform density distribution will be applied. Simultaneously, the effect of wax is also examined. Wax is applied to the samples by melting it through heating. As observed in Table 4.8, the density measurements of the large samples show minimal difference before and after the application of wax, while the small samples exhibit a slight change in density. Therefore, the influence of wax on large samples can be thought as small, while for small sample, the influence should be considered.

Table 4.7: Test for density distribution

Atmosphere	Mass _{air} (g)	Mass _{water} (g)	Density (g/cm ³)	Relative Density (%)	Position
Argon (< 18 μm)	9.429	8.192	7.60	95.00	upper-left
	8.271	7.192	7.64	95.53	lower-left
	6.967	6.058	7.64	95.52	upper-right
	6.267	5.444	7.59	94.90	lower-right
Argon (< 25 μm)	9.595	8.371	7.82	97.69	upper-left
	9.060	7.900	7.79	97.34	lower-left
	6.785	5.921	7.83	97.87	upper-right
	6.742	5.874	7.74	96.80	lower-right
Vacuum (< 25 μm)	5.578	4.848	7.62	95.23	upper-left
	10.57	9.184	7.60	95.04	lower-left
	6.633	5.758	7.56	94.47	upper-right
	6.830	5.926	7.53	94.16	lower-right

Table 4.8: The effect of wax application on density

Size	Sample	Density (g/cm ³)	Relative Density (%)
2×2×2 cm ³	Wax	7.63	95.38
2×2×2 cm ³	No Wax	7.64	95.54
1×1×1 cm ³	Wax	7.79	97.43
1×1×1 cm ³	No Wax	7.70	96.21

Although the Archimedes method theoretically tends to yield slightly higher density values due to external factors such as air bubbles and temperature variations, considering the inaccuracies in the sample's shape and sample defects, the sample's density distribution remains relatively uniform (as shown in Table 4.7). Therefore, for the purposes of this study, the density results obtained using the Archimedes method will be adopted as research data.

4.4.2. Dimensional Changes

For dimension measurements, four large samples (2×2×2 cm³ printing model) plus three small samples (1×1×1 cm³ printing model) are tested. The measurements are conducted using calipers, and this process involves selecting three adjacent faces of each cube and measuring three points on each face, as illustrated in Figure 3.6. The detailed measurement results are presented in Table 4.9.

Table 4.9: Dimensional Measurement Results of Samples with Varying Sizes

Model	Sample	After Sintering			Before Sintering			Change (%)		
		X/cm	Y/cm	N/cm	X/cm	Y/cm	N/cm	X/cm	Y/cm	N/cm
2×2×2 cm ³	6	1.75 ± 0.0046	1.77 ± 0.0093	1.71 ± 0.0060	2.05	2.08	2.04	-13%	-15%	-16%
	7	1.72 ± 0.0075	1.77 ± 0.0133	1.67 ± 0.0010	2.03	2.05	2.02	-15%	-14%	-17%
	8	1.74 ± 0.0055	1.74 ± 0.0040	1.67 ± 0.0040	2.06	2.04	2.06	-15%	-15%	-19%
	9	1.73 ± 0.0083	1.74 ± 0.0121	1.66 ± 0.0100	2.03	2.05	2.05	-15%	-15%	-19%
1×1×1 cm ³	1	0.87 ± 0.0006	0.87 ± 0.0006	0.82 ± 0.0006	1.01	1.03	1.04	-14%	-16%	-21%
	2	0.86 ± 0.0006	0.87 ± 0.0010	0.83 ± 0.0006	1.02	1.02	1.04	-16%	-15%	-20%
	3	0.89 ± 0.0067	0.86 ± 0.0021	0.82 ± 0.0006	1.03	1.02	1.04	-14%	-16%	-21%

The results in Table 4.9 indicate that the shrinkage along ND is greater than that along XD and the YD, as shown in Figure 3.6. For both large and small samples, the shrinkage in the X and Y directions is approximately 15%. However, in the N direction, the shrinkage for small samples is around 20%, while for large samples, it ranges from 16% to 19%.

The approximately 4% higher shrinkage in the ND compared to the XD and YD can be attributed to several factors. First, during high-temperature sintering, the material softens, and the combined effects of the material's own weight and internal stresses within the printed part lead to additional shrinkage [52]. Second, the N direction is not consistently oriented upward during sintering, resulting in voids between adjacent layers in this direction. These voids reduce the packing density, making compression more likely. Third, binder jetting may cause particle splashing, which leads to the formation of subsurface depletion zones [100]. These zones contribute to residual voids due to insufficient compaction of subsequent powder layers, which are likely introduced during the printing process. Furthermore, the incomplete penetration of binder during printing in the ND can result in higher interlayer porosity [101]. Lastly, as the samples densify during sintering, the collapse of pores can further exacerbate shrinkage in the ND.

4.5. Mechanical Analysis

4.5.1. Hardness

Hardness testing was conducted on samples from the same batch as those in Table 4.7 to minimize confounding factors. Using a Vickers hardness tester, both the indentation images and hardness values of the sample surfaces were obtained. The tested surfaces included the sample surface (XY plane) and cross-section (Z-axis), and all tested planes are ground and polished. Figure 4.20 shows randomly selected hardness test results from multiple measurements, corresponding to the hardness values at specific locations on the XY plane of three different samples. Combined with the data in Table 4.10, the vacuum-sintered samples with particle sizes smaller than 25 microns exhibited the highest hardness, with an average hardness of 283 HV10 on the XY plane and approximately 294.3 HV10 in the longitudinal direction. The argon-sintered samples with particle sizes smaller than 25 microns had intermediate hardness, with an average hardness of 117.9 HV10 on the XY plane and approximately 124.8 HV10 in the longitudinal direction. The argon-sintered samples with particle sizes smaller than 18 microns showed the lowest hardness, with an average of 103.17 HV10 on the XY plane and approximately 107.4 HV10 in the longitudinal direction.

Table 4.10: Average hardness value of 3 samples (HV10)

Sample	XY Plane (HV10)	Z-axis (HV10)
< 25 μm in vacuum	283.0 ± 14.49	294.3 ± 4.20
< 18 μm in Ar	117.9 ± 1.92	124.8 ± 0.46
< 25 μm in Ar	103.2 ± 2.15	107.4 ± 1.45

Figure 4.21 illustrates the relationship among the powder particle size, sintering atmosphere, the Vickers hardness, grain size, and relative density of the samples. The grain size can be measured using the

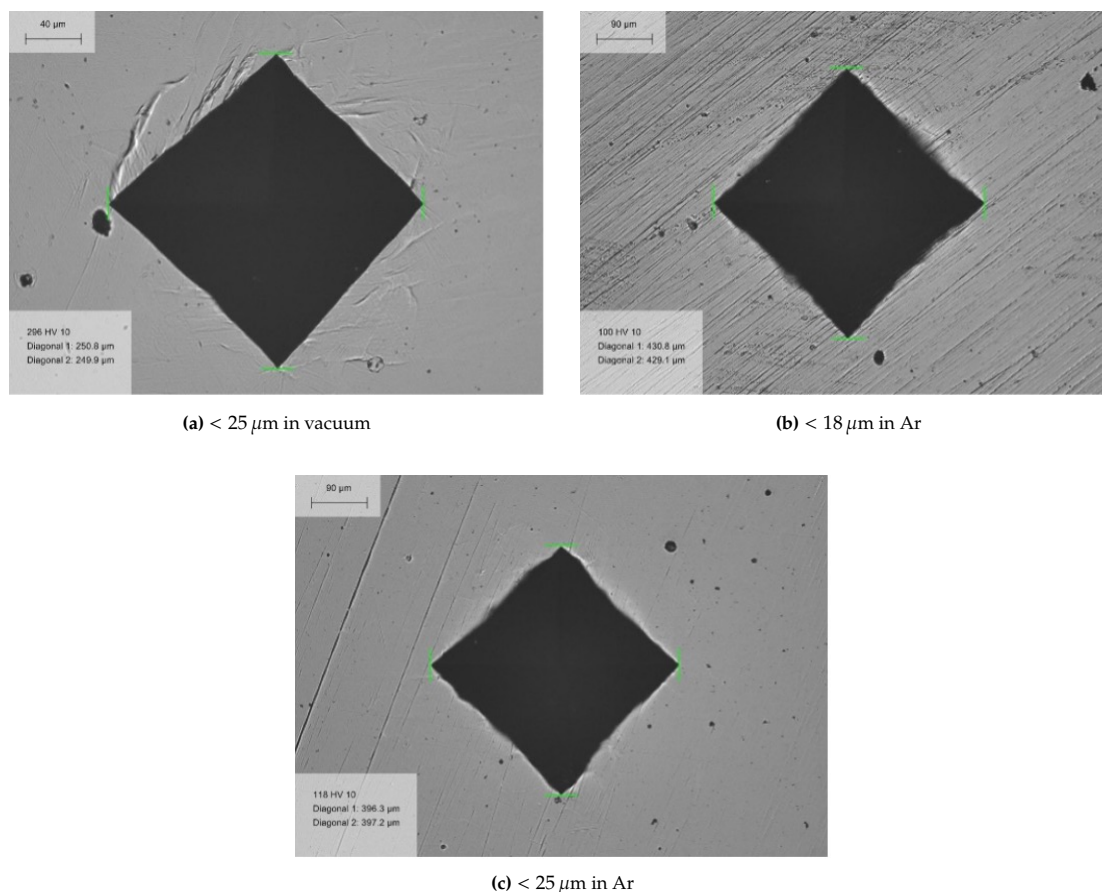


Figure 4.20: Comparison of the indentations for the three samples

intercept method with software such as ImageJ. Figure 4.22 provides a schematic representation of the grain size analysis conducted on a $25 \mu\text{m}$ sample sintered under an argon atmosphere. By drawing lines of a specific length across the grains, the average length of line segments required to intersect a single grain can be calculated, which represents the average grain size. It is important to note that, during the actual counting process, line segments that do not fully intersect complete grains at their endpoints are generally counted as one grain. Additionally, the focus of the measurement is on the number of grain boundary intersections rather than the total number of grains. To ensure accuracy, the total number of grains intersected in the given direction should be as large as possible, with the cumulative number of grains counted across multiple lines exceeding 100. In this study, the data used represent the average grain size based on four intercept lines. However, it is difficult to accurately process features such as blurred grain boundaries from images, Therefore, the result is less intuitive than the other two events that are analyzed directly from numerical data.

The data shows that as the particle size increases and the sintering atmosphere changes from argon (AR) to vacuum (VAC), there is a notable increase in hardness, with the highest value of 288.63 HV10 observed in the vacuum-sintered sample with a $25 \mu\text{m}$ particle size. However, the relative density remains relatively stable across different conditions, fluctuating around 95%. In contrast, the grain size shows a decreasing trend as the sintering environment transitions from argon to vacuum, with the grain size decreasing from $75 \mu\text{m}$ in the $18 \mu\text{m}$ AR sample to $57 \mu\text{m}$ in the $25 \mu\text{m}$ vacuum-sintered sample. This suggests that the sintering atmosphere significantly influences the microstructural evolution and mechanical properties of the samples, with vacuum sintering promoting higher hardness while limiting

grain growth.

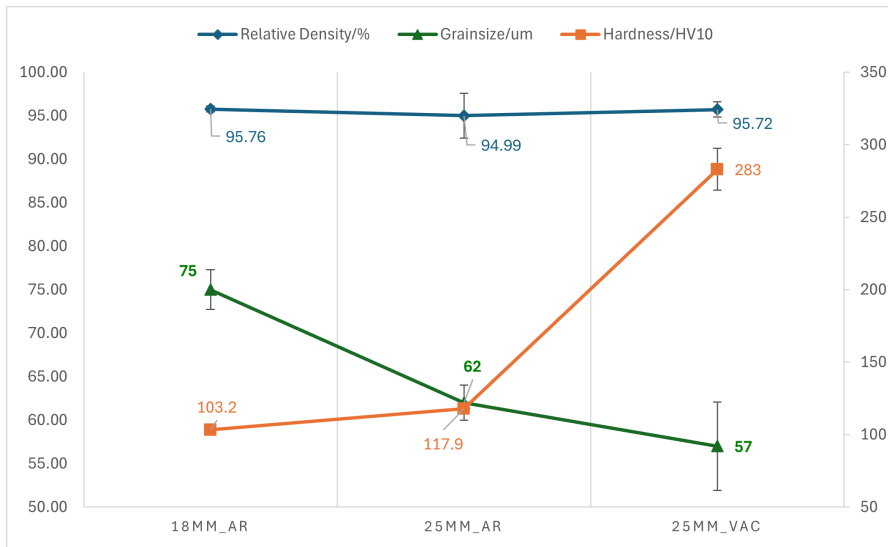


Figure 4.21: Relationship between different sintering atmosphere and hardness, grain size and relative density

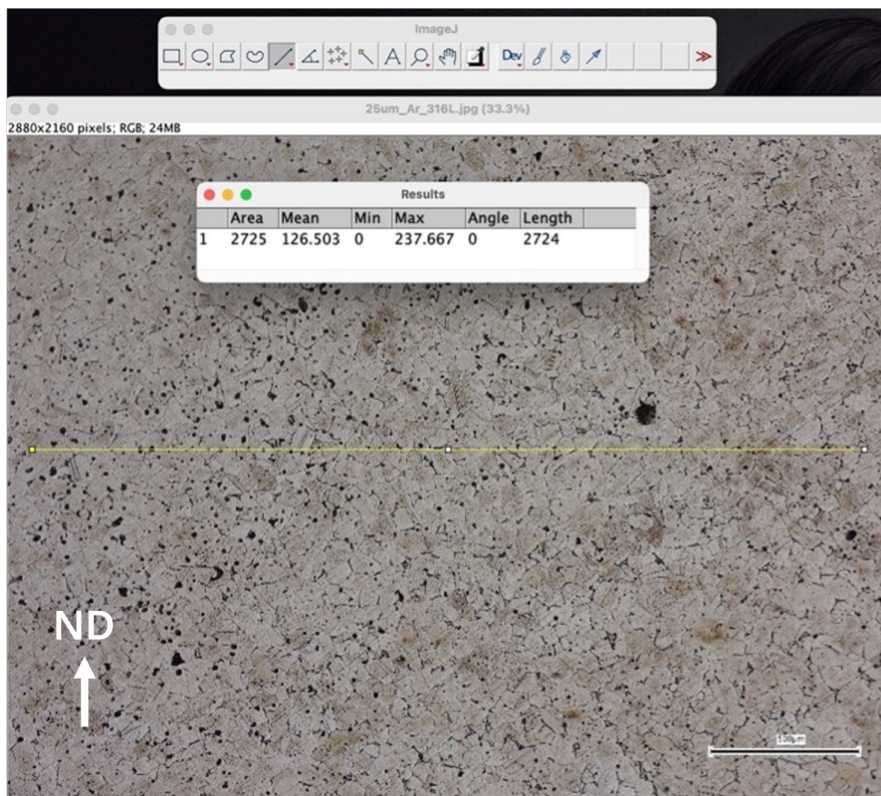


Figure 4.22: Grain size measurement through Image J

Table 4.11 lists five studies on BJ-manufactured 316L stainless steel, all employing sintering as the post-processing method without HIP or MIM. The hardness of the samples sintered in argon atmosphere is lower than the reported values, while vacuum-sintered samples exhibit significantly higher hardness. This can be attributed to higher density, finer grain size, lower porosity, and a greater presence of delta ferrite along with more prevalent twinning crystals in the austenitic matrix. In the right image of

Figure 4.23b, the vacuum-sintered sample exhibits smoother grain boundaries than the sample in Ar (Figure 4.23a), with the black precipitates along the grain edges identified as ferrite.

The formation of ferrite during vacuum sintering of 316L stainless steel can be attributed to several factors. First, differential distribution of alloying elements, such as the higher concentration of ferrite stabilizers (Cr, Mo) in ferritic regions and a lower concentration of austenite stabilizers (Ni), promotes ferrite formation. Second, the deliberate addition of alloying elements (such as Cr, Mo and Ni) to the pre-alloyed powder influences the phase composition, while the use of the Schaeffler diagram enables precise control over the balance of ferrite and austenite phases. These factors collectively contribute to the enhanced ferrite content in vacuum-sintered 316L stainless steel [102]. Moreover, Mariappan et al [103] found that stainless steel sintered in argon atmosphere exhibit limited ferrite formation compared to other conditions. Thus, it should be that both ferrite and twinning crystals within Vacuum-sintered samples contribute to the high hardness, while the lack of hard phases and voids within Ar-sintered samples can reduce the hardness.

Table 4.11: Vicker hardness values from 5 studies

Author	Hardness (HV)	Reference
Mirzababaei et al.	155–165	[104]
Tillmann et al.	104–143	[105]
Lecis et al.	137–178	[106]
ExOne	119–127	[107]
This Study	111–220	-

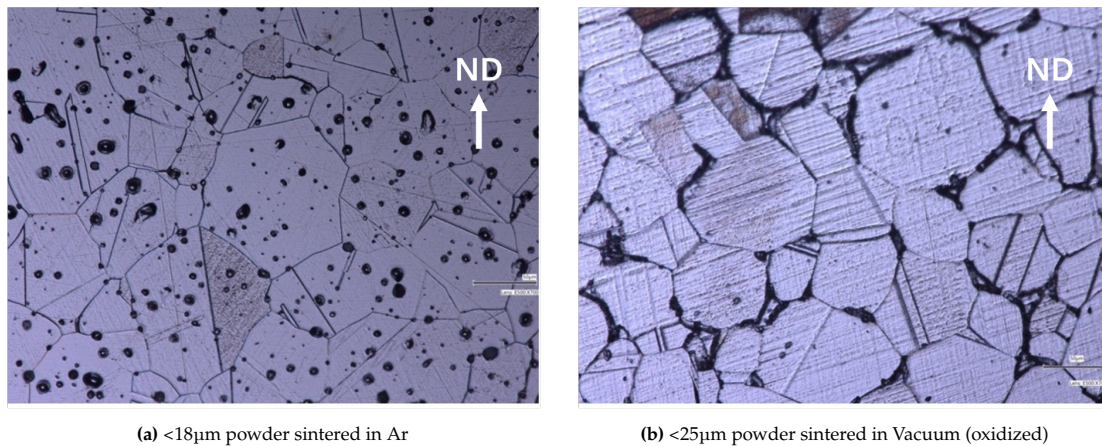


Figure 4.23: Microstructure of samples within different sintering atmosphere

4.5.2. Compression Tests

The compression tests were conducted using a Zwick Z100 machine, with a maximum load capacity of 100 kN. Due to limitations in sample quantity and geometry, three compression tests were performed. In all tests, the samples did not exhibit failure even after reaching the 100 kN load. Figure 4.24 presents the data from one of these tests. Since the samples did not fully fail, the figure does not provide sufficient information for a comprehensive analysis. However, from the obvious deformation (Figure 4.25), significant internal voids were identified within the samples. Table 4.12 presents the dimensional data of the three samples before and after compression.

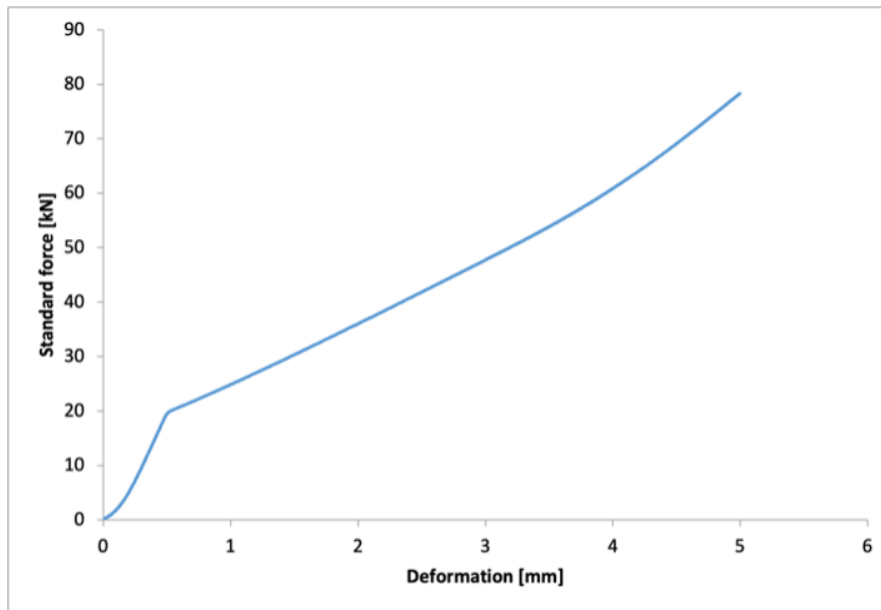


Figure 4.24: Compression test on complete cubic sample

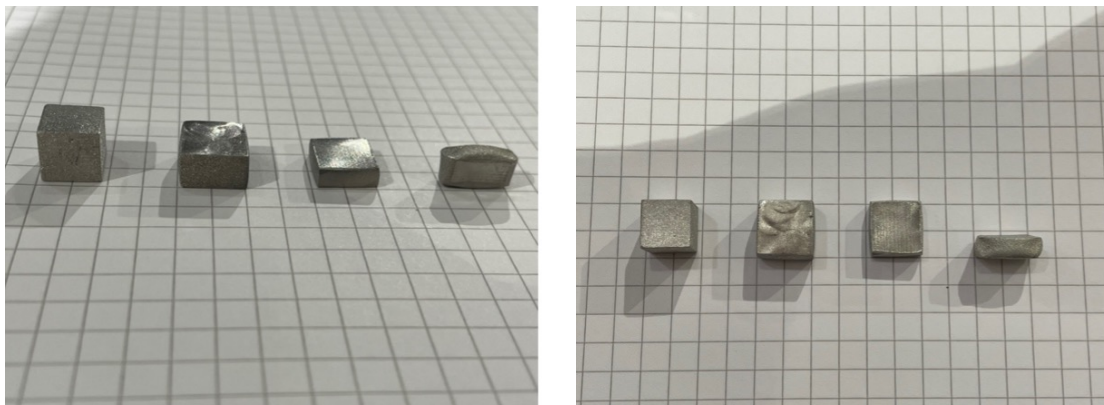


Figure 4.25: Complete sample, N-compressed complete sample, X/Y-compressed half sample 1, X/Y-compressed half sample 2

Table 4.12: Sample dimension change ("*" means after compression test), unit: mm

Sample	N	N*	X	X*	Y	Y*
N-Complete	8.62	6.03	8.63	10.52	8.22	10.56
X/Y-Half	8.23	10.44	4.54	3.28	8.59	10.01
X/Y-Half	8.68	11.84	8.12	6.70	3.71	4.14
	ΔN		ΔX		ΔY	
N-Complete	-2.59		+1.89		+2.34	
X/Y-Half	+2.21		-1.26		+1.42	
X/Y-Half	+3.16		-1.42		+0.43	

Due to the limited number of samples, a small cube was evenly cut in half for the experiment Figure 4.25 shows, from left to right: the intact sample, the intact sample compressed in the ND, one half of the sample compressed in the XD or YD, and the other half compressed in the XD or YD. Based on the grid lines in the background, the dimensional changes before and after compression are significant. As indicated in Table 18, the deformation in the ND is consistently the largest among the three directions. Furthermore, even at the maximum load of 100 kN, the sample appears to be capable of further

compression, suggesting the presence of considerable internal voids. However, considering the density and hardness data mentioned earlier, it is likely that the voids are primarily between layers rather than due to excessively high overall porosity. The larger interlayer voids may be attributed to several factors during the printing process, including insufficient compaction by the powder roller, inadequate binder saturation levels, and suboptimal interactions between the binder and the powder.

5

Conslusions

This study focuses on the 316L stainless steel parts produced by Concr3de using binder jetting technology. Through the adjustment of process parameters, mechanical testing, and microstructural characterization, deficiencies in the printed samples were identified. By optimizing these parameters, improvements in the mechanical performance of the printed parts were achieved. The main conclusions are as follows:

1. With the current binder, the optimal printing performance has been achieved using a layer height of 0.1 mm, a feed height of 0.18 mm, and a roller speed of 50%. However, the settings for X-speed and spread speed should be adjusted based on the specific machine configuration. For instance, on the Mode 2000 machine, X-speed should be maintained between 30% and 50%, while spread speed should be set within the range of 20% to 30%. In contrast, for the Chiron machine, the recommended settings are X-speed at 20% and spread speed at 40%.
2. According to the results of TGA test and density analysis, the appropriate debinding and sintering parameters for Concr3de's BJ 316L stainless steel samples are determined to be 450 °C for 5 hours for debinding and 1400 °C (or 1410 °C) for 5 hours for sintering. Under these conditions, the relative density of the sintered samples stabilized above 94%, with a maximum value reaching approximately 98%. Sintering atmosphere also influence material performance. In this study, samples sintered within vacuum own fewer pores, higher hardness and a more homogeneous microstructure compared to those in argon.
3. Several issues can be encountered during the printing process, resulting in suboptimal mechanical properties of the samples:
 - Binder and powder provided by the company exhibit suboptimal compatibility, which results in inadequate bonding along ND within the samples. Thus, the insufficient interlayer adhesion creates large compressible space, and it ultimately compromises sample performance in compression test.
 - Machine instability affect sample performance. Issues include, but are not limited to bind-clogging printhead, suboptimal powder bed morphology due to powder leakage and roller scratch. Additionally, the interaction between binder droplets and powder particles remains insufficiently understood and requires further investigation.
 - Possible solutions include reducing the binder's volatility and viscosity, redesigning the printing platform, improving powder bed compaction through roller adjustments, and minimizing the number of powder recycling cycles to enhance printing consistency and part quality.
4. Black voids can be observed in the microstructure of sintered samples, which are suspected to be either Type III pores during sintering or pits caused by pitting corrosion. Type III pores are difficult to eliminate through sintering and lead to larger interlayer voids, particularly in the

vertical direction, resulting in significant shrinkage and impacting the material's mechanical properties. Pitting corrosion may be caused by excessively high ambient humidity. Additionally, the sintering atmosphere can affect material performance. Samples sintered within vacuum own fewer pores, higher hardness and a more homogeneous microstructure compared to those in argon. Hardness testing confirmed that samples sintered in a vacuum had superior hardness.

Knowledge Gap and Further Research

6.1. Knowledge gap

1. In BJP processing, the printing process serves as the initial step in the production of the final product. During the powder spreading stage, issues such as poor powder bed deposition, powder leakage, and suboptimal powder bed density can significantly impact subsequent steps. Parameters such as X-speed, layer thickness, and roller spreading speed critically affect the integrity, accuracy, and density of the green parts. However, the intrinsic flowability of the powder and its relationship with these parameters could not be thoroughly investigated in this study. Therefore, understanding the influence of powder spreading parameters on the quality of the printed parts is of great importance.

2. In this study, the interaction between the binder and SS 316L remains unclear. Although a relatively suitable 3P waveform was employed, a binder-jetting system was designed to match this binder, and the X and Y velocities of the print head were adjusted, the green parts still failed to achieve satisfactory printing accuracy or morphology. Thus, further investigation into the binder-powder interaction is necessary.

3. Observations of as-sintered samples under SEM and OM revealed black regions resembling voids. However, their nature and origin remain unclear. If these voids are caused by pitting corrosion, it raises important questions about why pitting corrosion occurs in SS 316L, a material known for its excellent corrosion resistance. Investigating the mechanisms behind this phenomenon is essential.

6.2. Future Research

- Conduct a detailed investigation into the effects of printing parameters on the printing process. This objective can be divided into two key aspects:
 - Investigate the interaction between binder droplets and metallic powders, including SS 316L. Specifically, examine the wetting behavior of the binder on the powder surface and its penetration into the powder. This will provide insights into improving the bonding quality of metallic powders, which is crucial for developing subsequent post-treatment processes.
 - Explore alternative post-treatment methods beyond sintering. Considering the long sintering durations and the stringent requirements for sintering atmospheres in this experiment, research into new sintering techniques or entirely different post-treatment methods is necessary, focusing on economic cost, time efficiency, and overall performance.
- Develop new material systems to enhance the binder-jetting process.
 - The binder used in this experiment showed high chemical stability and viscosity, but these properties resulted in suboptimal binder jetting, negatively impacting the printing process.

-
- Investigate new binder materials, optimize their physicochemical properties, and explore alternative metallic powders. The goal is to identify compatible binder-metal combinations that improve bonding performance while reducing operational complexity, benefiting both laboratory research and industrial production.

References

- [1] William E Frazier. "Metal additive manufacturing: a review". In: *Journal of Materials Engineering and performance* 23 (2014), pp. 1917–1928.
- [2] Nannan Guo and Ming C Leu. "Additive manufacturing: technology, applications and research needs". In: *Frontiers of mechanical engineering* 8 (2013), pp. 215–243.
- [3] Elke Vorndran, Claus Moseke, and Uwe Gbureck. "3D printing of ceramic implants". In: *Mrs Bulletin* 40.2 (2015), pp. 127–136.
- [4] Yuhua Song et al. "Manufacture of the die of an automobile deck part based on rapid prototyping and rapid tooling technology". In: *Journal of materials processing technology* 120.1-3 (2002), pp. 237–242.
- [5] Charles L Thomas et al. "Rapid prototyping of large scale aerospace structures". In: *1996 IEEE Aerospace Applications Conference. Proceedings*. Vol. 4. IEEE. 1996, pp. 219–230.
- [6] Kaufui V Wong and Aldo Hernandez. "A review of additive manufacturing". In: *International scholarly research notices* 2012.1 (2012), p. 208760.
- [7] Jan Holmström et al. "Rapid manufacturing in the spare parts supply chain: Alternative approaches to capacity deployment". In: *Journal of manufacturing technology management* 21.6 (2010), pp. 687–697.
- [8] William E Frazier. "Metal additive manufacturing: a review". In: *Journal of Materials Engineering and performance* 23 (2014), pp. 1917–1928.
- [9] Xiangyuan Ren et al. "3D gel-printing—An additive manufacturing method for producing complex shape parts". In: *Materials & Design* 101 (2016), pp. 80–87.
- [10] Dawn White. *Ultrasonic object consolidation*. US Patent 6,519,500. Feb. 2003.
- [11] Dawn White and David EE Carmein. *Ultrasonic object consolidation system and method*. US Patent 6,463,349. Oct. 2002.
- [12] Yun Bai and Christopher B Williams. "An exploration of binder jetting of copper". In: *Rapid Prototyping Journal* 21.2 (2015), pp. 177–185.
- [13] Truong Do et al. "Improving structural integrity with boron-based additives for 3D printed 420 stainless steel". In: *Procedia Manufacturing* 1 (2015), pp. 263–272.
- [14] Yi Zhang et al. "Additive manufacturing of metallic materials: a review". In: *Journal of Materials Engineering and Performance* 27 (2018), pp. 1–13.
- [15] Anketa Jandyal et al. "3D printing—A review of processes, materials and applications in industry 4.0". In: *Sustainable Operations and Computers* 3 (2022), pp. 33–42.
- [16] Truong Do, Patrick Kwon, and Chang Seop Shin. "Process development toward full-density stainless steel parts with binder jetting printing". In: *International Journal of Machine Tools and Manufacture* 121 (2017), pp. 50–60.
- [17] Li Sun et al. "Densification and properties of 420 stainless steel produced by three-dimensional printing with addition of Si 3 N 4 powder". In: (2009).
- [18] Bruno Verlee, Thierry Dormal, and Jacqueline Lecomte-Beckers. *Density and porosity control of sintered 316L stainless steel parts produced by additive manufacturing*. 2012.
- [19] Emanuel Sachs, Michael Cima, and James Cornie. "Three-dimensional printing: rapid tooling and prototypes directly from a CAD model". In: *CIRP annals* 39.1 (1990), pp. 201–204.
- [20] Ben Utela et al. "A review of process development steps for new material systems in three dimensional printing (3DP)". In: *Journal of Manufacturing Processes* 10.2 (2008), pp. 96–104.

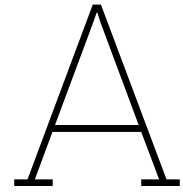
- [21] R Shivpuri et al. "Evaluation of 3D printing for dies in low volume forging of 7075 aluminum helicopter parts". In: *Rapid Prototyping Journal* 11.5 (2005), pp. 272–277.
- [22] I Gibson, D Rosen, and B Stucker. "Standard Terminology for Additive Manufacturing Technologies". In: *Rapid Manufacturing Association* 2 (2013), pp. 10–12.
- [23] Ming Li et al. "Metal binder jetting additive manufacturing: a literature review". In: *Journal of Manufacturing Science and Engineering* 142.9 (2020), p. 090801.
- [24] WEI Qing-song et al. "Development and Prospect of Metal Binder Jetting Additive Manufacturing Technology". In: *PACKAGING ENGINEERING* 42.18 (2021), pp. 103–119.
- [25] C Lindemann et al. "Analyzing Product Lifecycle Costs for a Better Understanding of Cost Drivers in Additive Manufacturing". In: *23rd Annual International Solid Freeform Fabrication Symposium*. Vol. 23. 2012.
- [26] Mohsen Ziaee and Nathan B Crane. "Binder jetting: A review of process, materials, and methods". In: *Additive Manufacturing* 28 (2019), pp. 781–801.
- [27] Amir Mostafaei et al. "Binder jet 3D printing—Process parameters, materials, properties, modeling, and challenges". In: *Progress in Materials Science* 119 (2021), p. 100707.
- [28] J Yoo et al. "Structural ceramic components by 3D printing". In: *1993 International Solid Freeform Fabrication Symposium*. 1993.
- [29] Scott A Uhland et al. "Strength of green ceramics with low binder content". In: *Journal of the American Ceramic Society* 84.12 (2001), pp. 2809–2818.
- [30] Ian Gibson et al. "Binder jetting". In: *Additive manufacturing technologies* (2021), pp. 237–252.
- [31] Truong Do et al. "Additively manufactured full-density stainless steel 316L with binder jet printing". In: *International Manufacturing Science and Engineering Conference*. Vol. 51357. American Society of Mechanical Engineers. 2018, V001T01A017.
- [32] J Abenojar et al. "Atmosphere influence in sintering process of stainless steels matrix composites reinforced with hard particles". In: *Composites Science and Technology* 63.1 (2003), pp. 69–79.
- [33] Ravi K Enneti et al. "Sintering of WC-12% Co processed by binder jet 3D printing (BJ3DP) technology". In: *International Journal of Refractory Metals and Hard Materials* 71 (2018), pp. 28–35.
- [34] Matthew P Watters and Michelle L Bernhardt. "Modified curing protocol for improved strength of binder-jetted 3D parts". In: *Rapid Prototyping Journal* 23.6 (2017), pp. 1195–1201.
- [35] Sanjay Joshi et al. "Post Processing". In: *Additive Manufacturing with Metals: Design, Processes, Materials, Quality Assurance, and Applications*. Springer, 2023, pp. 567–589.
- [36] Haidong Wu et al. "Effect of the particle size and the debinding process on the density of alumina ceramics fabricated by 3D printing based on stereolithography". In: *Ceramics International* 42.15 (2016), pp. 17290–17294.
- [37] MN Rahaman. "Kinetics and mechanisms of densification". In: *Sintering of advanced materials*. Elsevier, 2010, pp. 33–64.
- [38] Mohd Rhafiq Mazlan et al. "Necking mechanism under various sintering process parameters—a review". In: *journal of materials research and technology* 23 (2023), pp. 2189–2201.
- [39] Byung-Nam Kim et al. "Theoretical analysis of experimental densification kinetics in final sintering stage of nano-sized zirconia". In: *Journal of the European Ceramic Society* 39.4 (2019), pp. 1359–1365.
- [40] Suk-Joong L Kang. *Sintering: densification, grain growth and microstructure*. Elsevier, 2004.
- [41] WD Kingery. "Densification during sintering in the presence of a liquid phase. I. Theory". In: *Journal of Applied Physics* 30.3 (1959), pp. 301–306.
- [42] Mohsen Ziaee, Eric M Tridas, and Nathan B Crane. "Binder-jet printing of fine stainless steel powder with varied final density". In: *Jom* 69 (2017), pp. 592–596.
- [43] Fazilet Güngör and Nuran Ay. "The effect of particle size of body components on the processing parameters of semi transparent porcelain". In: *Ceramics International* 44.9 (2018), pp. 10611–10620.

- [44] Chuantong Chen et al. "Effect of size and shape of Ag particles for mechanical properties of sintered Ag joints evaluated by micro-compression test". In: *2017 International Conference on Electronics Packaging (ICEP)*. IEEE. 2017, pp. 130–134.
- [45] ZY Liu, TB Sercombe, and GB Schaffer. "The effect of particle shape on the sintering of aluminum". In: *Metallurgical and Materials Transactions A* 38 (2007), pp. 1351–1357.
- [46] Ashwath Kumar et al. "Effects of hot isostatic pressing on copper parts fabricated via binder jetting". In: *Procedia Manufacturing* 10 (2017), pp. 935–944.
- [47] Saereh Mirzababaei and Somayeh Pasebani. "A review on binder jet additive manufacturing of 316L stainless steel". In: *Journal of Manufacturing and Materials Processing* 3.3 (2019), p. 82.
- [48] Fahimeh Dini et al. "A review of binder jet process parameters; powder, binder, printing and sintering condition". In: *Metal Powder Report* 75.2 (2020), pp. 95–100.
- [49] Xinyuan Lv et al. "Binder jetting of ceramics: Powders, binders, printing parameters, equipment, and post-treatment". In: *Ceramics International* 45.10 (2019), pp. 12609–12624.
- [50] Truong Do, Patrick Kwon, and Chang Seop Shin. "Process development toward full-density stainless steel parts with binder jetting printing". In: *International Journal of Machine Tools and Manufacture* 121 (2017), pp. 50–60.
- [51] Hadi Miyajani et al. "Effect of fine powder particles on quality of binder jetting parts". In: *Additive Manufacturing* 36 (2020), p. 101587.
- [52] Amir Mostafaei et al. "Effect of powder size distribution on densification and microstructural evolution of binder-jet 3D-printed alloy 625". In: *Materials & Design* 162 (2019), pp. 375–383.
- [53] J Suwanprateeb, R Sanngam, and T Panyathanmaporn. "Influence of raw powder preparation routes on properties of hydroxyapatite fabricated by 3D printing technique". In: *Materials Science and Engineering: C* 30.4 (2010), pp. 610–617.
- [54] Peeyush Nandwana et al. "Powder bed binder jet 3D printing of Inconel 718: Densification, microstructural evolution and challenges". In: *Current Opinion in Solid State and Materials Science* 21.4 (2017), pp. 207–218.
- [55] Yun Bai, Grady Wagner, and Christopher B Williams. "Effect of particle size distribution on powder packing and sintering in binder jetting additive manufacturing of metals". In: *Journal of Manufacturing Science and Engineering* 139.8 (2017), p. 081019.
- [56] Yun Bai and Christopher B Williams. "An exploration of binder jetting of copper". In: *Rapid Prototyping Journal* 21.2 (2015), pp. 177–185.
- [57] Nancy Huang et al. "Review of Process–Structure–Property Relationships in Metals Fabricated Using Binder Jet Additive Manufacturing". In: *Metallography, Microstructure, and Analysis* (2023), pp. 1–23.
- [58] Hong Yong Sohn and C Moreland. "The effect of particle size distribution on packing density". In: *The Canadian Journal of Chemical Engineering* 46.3 (1968), pp. 162–167.
- [59] Guanxiong Miao et al. "A literature review on powder spreading in additive manufacturing". In: *Additive Manufacturing* (2022), p. 103029.
- [60] Hui Chen et al. "Powder-spreading mechanisms in powder-bed-based additive manufacturing: Experiments and computational modeling". In: *Acta Materialia* 179 (2019), pp. 158–171.
- [61] Mohsen Ziaee et al. "Fabrication of demineralized bone matrix/polycaprolactone composites using large area projection sintering (LAPS)". In: *Journal of Manufacturing and Materials Processing* 3.2 (2019), p. 30.
- [62] Usman Ali et al. "On the measurement of relative powder-bed compaction density in powder-bed additive manufacturing processes". In: *Materials & Design* 155 (2018), pp. 495–501.
- [63] Ming Li et al. "Ceramic binder jetting additive manufacturing: Relationships among powder properties, feed region density, and powder bed density". In: *Ceramics International* 47.17 (2021), pp. 25147–25151.

- [64] Guanxiong Miao et al. "Ceramic binder jetting additive manufacturing: Effects of granulation on properties of feedstock powder and printed and sintered parts". In: *Additive Manufacturing* 36 (2020), p. 101542.
- [65] AL Maximenko et al. "Modeling of effect of powder spreading on green body dimensional accuracy in additive manufacturing by binder jetting". In: *Powder Technology* 385 (2021), pp. 60–68.
- [66] Amir Mostafaei et al. "Microstructural evolution and mechanical properties of differently heat-treated binder jet printed samples from gas-and water-atomized alloy 625 powders". In: *Acta Materialia* 124 (2017), pp. 280–289.
- [67] Dan Soltman and Vivek Subramanian. "Inkjet-printed line morphologies and temperature control of the coffee ring effect". In: *Langmuir* 24.5 (2008), pp. 2224–2231.
- [68] Trenton Colton and Nathan B Crane. "Influence of droplet velocity, spacing, and inter-arrival time on line formation and saturation in binder jet additive manufacturing". In: *Additive Manufacturing* 37 (2021), p. 101711.
- [69] Michele Lanzetta and Emanuel Sachs. "Improved surface finish in 3D printing using bimodal powder distribution". In: *Rapid Prototyping Journal* 9.3 (2003), pp. 157–166.
- [70] Brian Derby. "Inkjet printing of functional and structural materials: fluid property requirements, feature stability, and resolution". In: *Annual Review of Materials Research* 40.1 (2010), pp. 395–414.
- [71] Kunlong Zhao et al. "Review of the types, formation mechanisms, effects, and elimination methods of binder jetting 3D-printing defects". In: *Journal of Materials Research and Technology* (2023).
- [72] Shane Agland and Simon M Iveson. "The impact of liquid drops on powder bed surfaces". In: *Chemeca 99 (27th: 1999: Newcastle, Australia)*. Institution of Engineers, Australia [Barton, ACT], 1999, pp. 218–224.
- [73] Heather N Emady et al. "Granule formation mechanisms and morphology from single drop impact on powder beds". In: *Powder technology* 212.1 (2011), pp. 69–79.
- [74] Yuanyuan Wang et al. "Simulation and experimental study of binder droplet infiltration in 3DP technology". In: *Modern Physics Letters B* 32.23 (2018), p. 1850272.
- [75] Issa Rishmawi, Mehrnaz Salarian, and Mihaela Vlasea. "Tailoring green and sintered density of pure iron parts using binder jetting additive manufacturing". In: *Additive Manufacturing* 24 (2018), pp. 508–520.
- [76] Ravi K Enneti and Kevin C Prough. "Effect of binder saturation and powder layer thickness on the green strength of the binder jet 3D printing (BJ3DP) WC-12% Co powders". In: *International Journal of Refractory Metals and Hard Materials* 84 (2019), p. 104991.
- [77] Ahmad Basalah, Shahrzad Esmaeili, and Ehsan Toyserkani. "On the influence of sintering protocols and layer thickness on the physical and mechanical properties of additive manufactured titanium porous bio-structures". In: *Journal of Materials Processing Technology* 238 (2016), pp. 341–351.
- [78] Zhao Chen et al. "Key technology of binder jet 3D printing". In: *Journal of Materials Engineering/Cailiao Gongcheng* 51.5 (2023).
- [79] Nathan B Crane. "Impact of part thickness and drying conditions on saturation limits in binder jet additive manufacturing". In: *Additive Manufacturing* 33 (2020), p. 101127.
- [80] Hadi Miyanaji, Shanshan Zhang, and Li Yang. "A new physics-based model for equilibrium saturation determination in binder jetting additive manufacturing process". In: *International Journal of Machine Tools and Manufacture* 124 (2018), pp. 1–11.
- [81] Peeyush Nandwana, Rangasayee Kannan, and Derek Siddel. "Microstructure evolution during binder jet additive manufacturing of H13 tool steel". In: *Additive Manufacturing* 36 (2020), p. 101534.
- [82] Amir Mostafaei et al. "Microstructural evolution and resulting properties of differently sintered and heat-treated binder-jet 3D-printed Stellite 6". In: *Materials Science and Engineering: C* 102 (2019), pp. 276–288.

- [83] Amir Mostafaei et al. "Powder bed binder jet printed alloy 625: Densification, microstructure and mechanical properties". In: *Materials & Design* 108 (2016), pp. 126–135.
- [84] Wei Gao et al. "The status, challenges, and future of additive manufacturing in engineering". In: *Computer-Aided Design* 69 (2015), pp. 65–89.
- [85] Yiwei Mao et al. "Effect of sintering temperature on binder jetting additively manufactured stainless steel 316L: densification, microstructure evolution and mechanical properties". In: *Journal of Materials Research and Technology* 22 (2023), pp. 2720–2735.
- [86] Robert Frykholm et al. "Solid state sintered 3-D printing component by using inkjet (binder) method". In: *Journal of the Japan Society of Powder and Powder Metallurgy* 63.7 (2016), pp. 421–426.
- [87] Yiwei Mao et al. "Binder jetting additive manufacturing of 316L stainless-steel green parts with high strength and low binder content: binder preparation and process optimization". In: *Journal of Materials Processing Technology* 291 (2021), p. 117020.
- [88] Alberto Cabo Rios et al. "Sintering anisotropy of binder jetted 316L stainless steel: part II—microstructure evolution during sintering". In: *Powder Metallurgy* 65.4 (2022), pp. 283–295.
- [89] Mengchen Xu et al. "Mechanical properties and microstructural characteristics of 316L stainless steel fabricated by laser powder bed fusion and binder jetting". In: *Journal of Materials Research and Technology* 24 (2023), pp. 4427–4439.
- [90] Terra. Tag. <https://www.terraanaliz.com/tag-1>. Accessed: 2024-01-08. 2024.
- [91] C. Gero. Laboratory furnace, graphite insulation (LHT GR). <https://www.carbolite-gero.com/products/vacuum-furnace/laboratory-furnaces/lhtg/>. Accessed: 2024-01-08. 2023.
- [92] Artec 3D. Artec Space Spider: Technical Specifications. [Online; accessed 01-August-2023]. 2023. URL: <https://www.artec3d.com/portable-3d-scanners/artec-spider%5C#specifications>.
- [93] International Organization for Standardization (ISO). ISO 2738: Sintered metal materials, excluding hardmetals — Permeable sintered metal materials — Determination of density, oil content, and open porosity. [Online; accessed 01-September-2024]. 2024. URL: <https://www.iso.org/obp/ui/#iso:std:iso:2738:en>.
- [94] Zhenhua Su et al. "Overcoming the penetration–saturation trade-off in binder jet additive manufacturing via rapid in situ curing". In: *Additive Manufacturing* 59 (2022), p. 103157.
- [95] Shu Cao et al. "Experimental and theoretical investigation on ultra-thin powder layering in three dimensional printing (3DP) by a novel double-smoothing mechanism". In: *Journal of materials processing technology* 220 (2015), pp. 231–242.
- [96] Yan Chen et al. "Real-time monitoring dislocations, martensitic transformations and detwinning in stainless steel: Statistical analysis and machine learning". In: *Journal of Materials Science & Technology* 92 (2021), pp. 31–39.
- [97] Moustafa El-Tahawy et al. "Different evolutions of the microstructure, texture, and mechanical performance during tension and compression of 316L stainless steel". In: *Metallurgical and Materials Transactions A* 51 (2020), pp. 3447–3460.
- [98] NE Gorji, R O'Connor, and D Brabazon. "XPS, XRD, and SEM characterization of the virgin and recycled metallic powders for 3D printing applications". In: *IOP Conference Series: Materials Science and Engineering*. Vol. 591. 1. IOP Publishing. 2019, p. 012016.
- [99] Masoud Atapour et al. "Corrosion of binder jetting additively manufactured 316L stainless steel of different surface finish". In: *Journal of The Electrochemical Society* 167.13 (2020), p. 131503.
- [100] Niranjana D Parab et al. "Real time observation of binder jetting printing process using high-speed X-ray imaging". In: *Scientific reports* 9.1 (2019), p. 2499.
- [101] Daniel Huber, Lucas Vogel, and Alfons Fischer. "The effects of sintering temperature and hold time on densification, mechanical properties and microstructural characteristics of binder jet 3D printed 17-4 PH stainless steel". In: *Additive Manufacturing* 46 (2021), p. 102114.
- [102] Z Brytan et al. "Characteristic of vacuum sintered stainless steels". In: *Journal of Achievements in Materials and Manufacturing Engineering* 33.2 (2009), pp. 126–134.

-
- [103] R Mariappan, S Kumaran, and T Srinivasa Rao. "Effect of sintering atmosphere on structure and properties of austeno-ferritic stainless steels". In: *Materials Science and Engineering: A* 517.1-2 (2009), pp. 328–333.
- [104] Saereh Mirzababaei, Brian K Paul, and Somayeh Pasebani. "Metal powder recyclability in binder jet additive manufacturing". In: *Jom* 72.9 (2020), pp. 3070–3079.
- [105] Wolfgang Tillmann et al. "Coatability of diamond-like carbon on 316L stainless steel printed by binder jetting". In: *Additive Manufacturing* 44 (2021), p. 102064.
- [106] Nora Lecis et al. "Effects of process parameters, debinding and sintering on the microstructure of 316L stainless steel produced by binder jetting". In: *Materials Science and Engineering: A* 828 (2021), p. 142108.
- [107] Weiping Chen et al. "Optimization of printing parameters to achieve high-density 316L stainless steel manufactured by binder jet 3D printing". In: *Journal of Materials Engineering and Performance* 32.8 (2023), pp. 3602–3616.



Printing Parameters

Table A.1: Session 1: Chiron Machine (1st printer)

Parameters	Data
X-speed	20%–50%
Spread Speed	40%–60%
Layer Height	0.1 mm
Feed Height	0.19 mm
Roller Speed	50%

Table A.2: Session 2: Type 2000 (2nd printer)

Parameters	Data
X-speed	30%–50%
Spread Speed	20%–30%
Layer Height	0.1 mm
Feed Height	0.18 mm
Roller Speed	50%

Table A.3: Session 3: Reassembled Chiron Machine (3rd printer)

Parameters	Data
X-speed	20%
Spread Speed	40%
Layer Height	0.1 mm
Feed Height	0.18 mm
Roller Speed	50%

B

Image of Samples



(a) Sintered Samples (with N-face up)

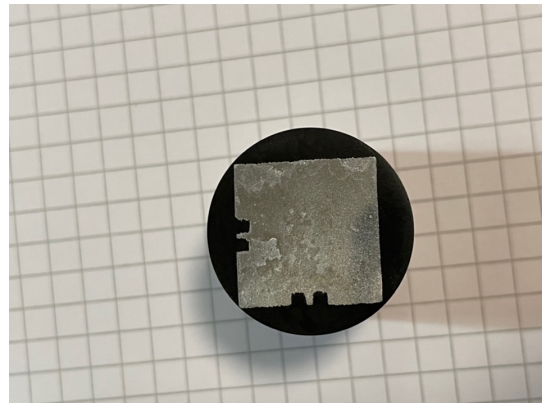


(b) Sintered samples with slight surface damage

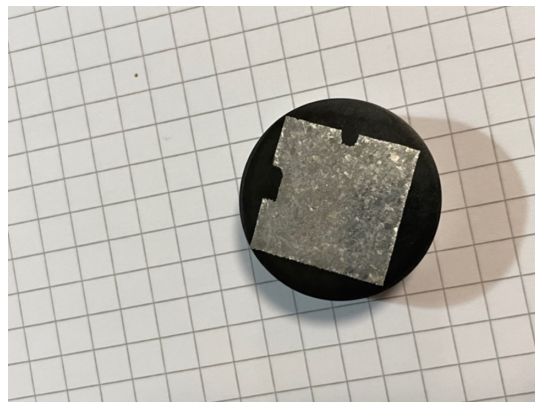
Figure B.1: As-sintered samples



(a) Polished samples for hardness test



(b) Etched 316L samples (<18 μm , in Ar):

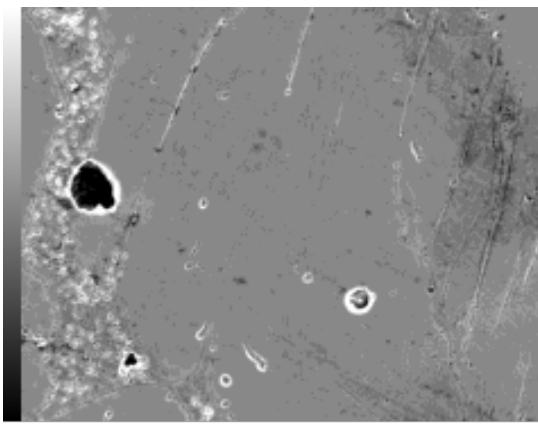


(c) Etched 316L samples (<25 μm , in Vacuum

Figure B.2: Samples for characterization

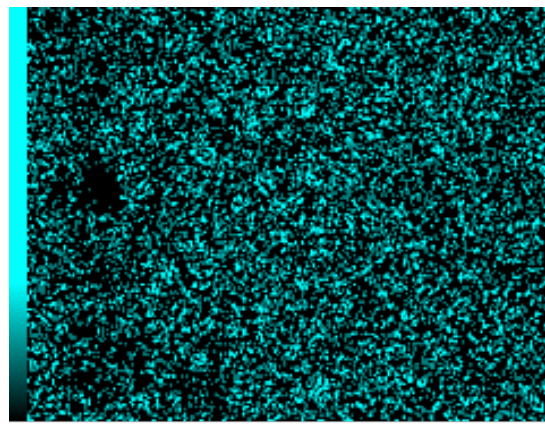
C

EDS Mapping



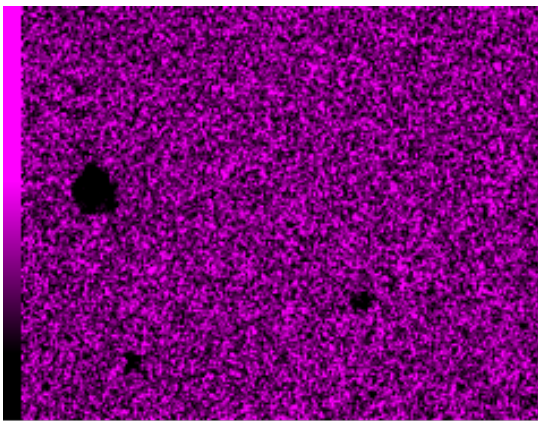
50 μm SED

(a) SED Image



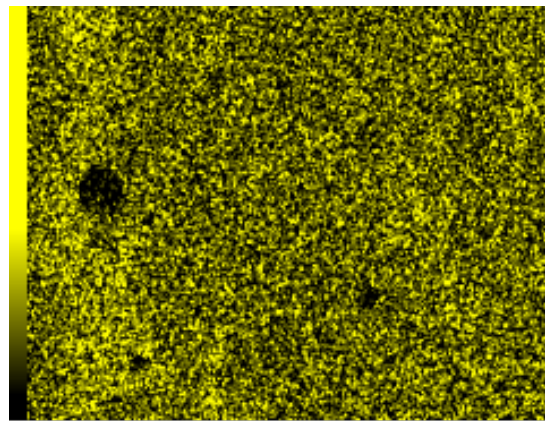
50 μm Ni K

(b) Ni K



50 μm Fe K

(c) Fe K



50 μm Cr K

(d) Cr K

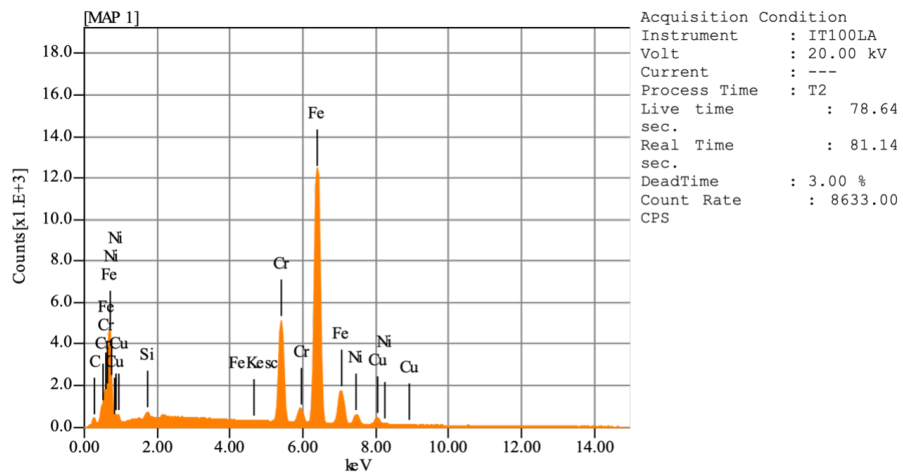
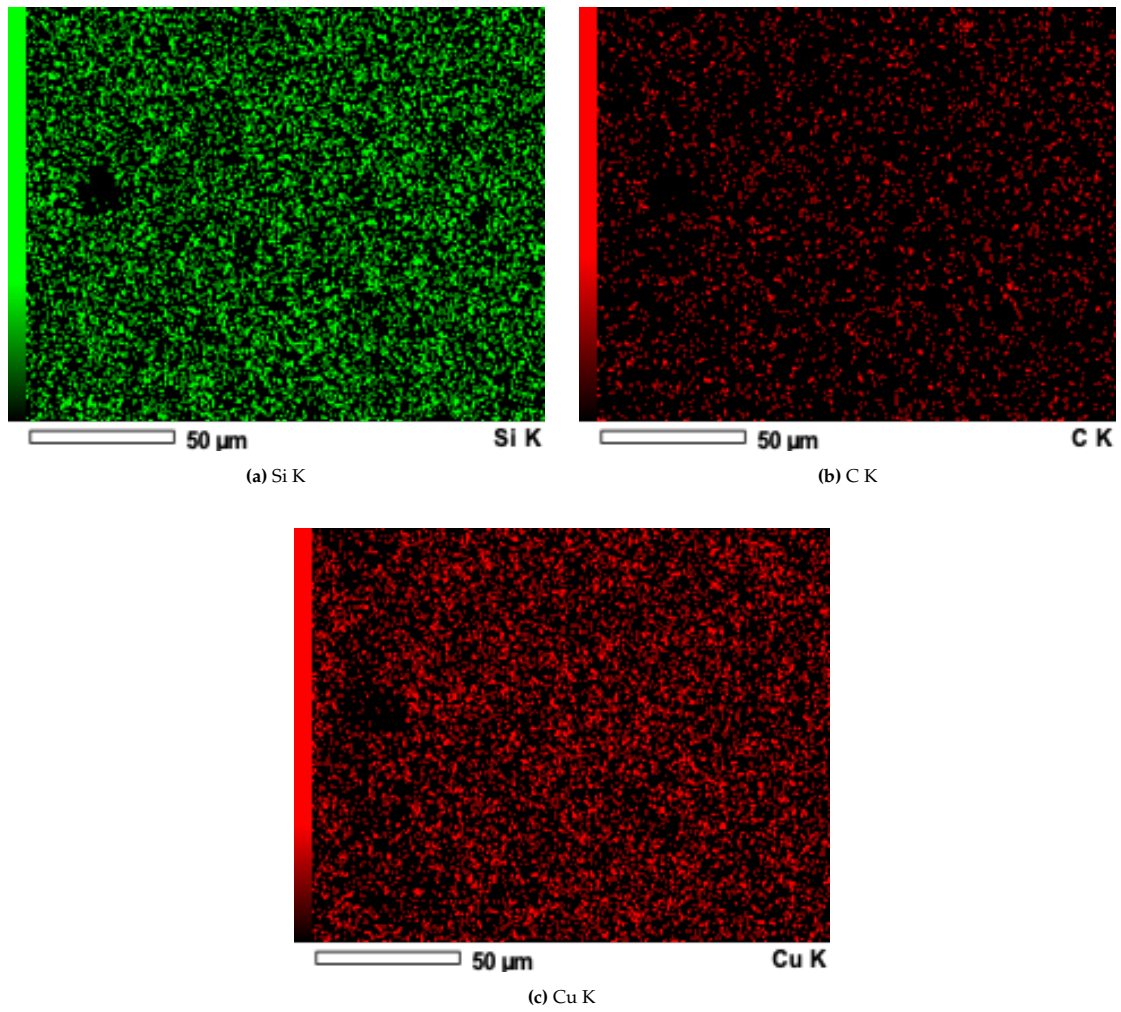


Figure C.3: Acquisition Condition